

Spectral Representation-based Reinforcement Learning

Chenxiao Gao

Georgia Tech

cgao@gatech.edu

Haotian Sun

Georgia Tech

hsun409@gatech.edu

Na Li

Harvard University

nali@seas.harvard.edu

Dale Schuurmans

Google DeepMind & University of Alberta Google DeepMind & Georgia Tech

schuurmans@google.com

Bo Dai

bodai@google.com

January 29, 2026

Abstract

In real-world applications with large state and action spaces, reinforcement learning (RL) typically employs function approximations to represent core components like the policies, value functions, and dynamics models. Although powerful approximations such as neural networks offer great expressiveness, they often present theoretical ambiguities, suffer from optimization instability and exploration difficulty, and incur substantial computational costs in practice. In this paper, we introduce the perspective of *spectral representations* as a solution to address these difficulties in RL. Stemming from the spectral decomposition of the transition operator, this framework yields an effective abstraction of the system dynamics for subsequent policy optimization while also providing a clear theoretical characterization. We reveal how to construct spectral representations for transition operators that possess latent variable structures or energy-based structures, which implies different learning methods to extract spectral representations from data. Notably, each of these learning methods realizes an effective RL algorithm under this framework. We also provably extend this spectral view to partially observable MDPs. Finally, we validate these algorithms on over 20 challenging tasks from the DeepMind Control Suite, where they achieve performances comparable or superior to current state-of-the-art model-free and model-based baselines. Our code is publicly released at <https://spectral-rl.github.io>.

Keywords— reinforcement learning, optimal control, representation learning, self-supervised learning, world models

Contents

1	Introduction	3
2	Preliminaries	5
3	The Framework of Spectral Representations	6
3.1	Spectral View of MDPs	6
3.2	Identifying Spectral Representations from Dynamics	8
3.2.1	Linear Formulation	9
3.2.2	Latent Variable Formulation	9
3.2.3	Energy-based Formulation	10
4	Algorithms for Learning Spectral Representations	12
4.1	Representations from Spectral Contrastive Learning	12
4.2	Representations from Variational Learning	14
4.3	Representations from Score Matching	14
4.4	Representations from Noise Contrastive Estimation	15
5	Reinforcement Learning with Spectral Representations	17
6	Spectral Representations in Partially Observable MDPs	20
7	Empirical Evaluations	21
7.1	Results with Proprioceptive Observations	23
7.2	Results with Visual Observations	24
7.3	Ablation Study and Analysis	25
8	Related Work	26
8.1	Reinforcement Learning with Representation Learning	26
8.2	Model-Based Reinforcement Learning	28
9	Closing Remarks	29
A	Online Exploration with Spectral Representations	40
B	Implementation Details	40
B.1	Implementation Details of Baseline Algorithms	40
B.2	Implementation Details of Spectral Representation-Based Algorithms	43

1 Introduction

Reinforcement Learning (RL) has emerged as a powerful tool in real-world applications that involve sequential decision-making [Degrave et al., 2022, Ouyang et al., 2022, Tang et al., 2025]. It formulates tasks based on Markov Decision Processes (MDPs) and learns an optimal policy that can maximize the expected cumulative return through interacting with an unknown environment [Sutton et al., 1998]. For MDPs with finite state and action spaces, known as the tabular case, efficient and convergent algorithms with well-defined theoretical sample complexities have been developed [Auer et al., 2008, Dann and Brunskill, 2015, Agrawal and Jia, 2017, Azar et al., 2017, Jin et al., 2018]. However, the optimization cost of these algorithms quickly becomes unacceptable as the volume of the state space and action space grows beyond tabular cases, even towards infinity in continuous state-action cases. To tackle such scalability challenges, modern RL algorithms employ function approximations to parameterize the core components in the pipeline [Jin et al., 2020, Yang et al., 2020, Long and Han, 2021]. Based on which component is approximated, these algorithms can be roughly classified into two categories: *model-free RL* and *model-based RL*. Model-free methods directly parameterize the policy and/or value functions, which are then optimized in an end-to-end fashion with trial-and-error interactions with the environment [Dai et al., 2018, Fujimoto et al., 2018, Haarnoja et al., 2018]. In contrast, model-based RL trains a surrogate dynamics model to capture the environment’s state transition, and the optimal policy can then be derived by planning or model predictive control using this learned model [Hafner et al., 2019a, Janner et al., 2019].

The architectural simplicity of modern model-free RL has enabled its successful integration with powerful function approximations (*e.g.*, deep neural networks) for policy/value function parameterization, leading to notable applications in diverse domains, such as generative model fine-tuning [Ouyang et al., 2022, Yang et al., 2024], video games [Mnih et al., 2013, Berner et al., 2019], and robotic control [Tang et al., 2025]. However, such expressive power also comes with theoretical challenges: with general function approximations, standard RL methods such as temporal-difference learning with off-policy data can diverge under some circumstances, a phenomenon known as the “deadly triad” [Sutton et al., 1998]. Furthermore, model-free RL is completely blind to the underlying dynamics, ultimately leading to a prohibitive sample complexity in practice [Fujimoto et al., 2018, Haarnoja et al., 2018].

Model-based RL, on the other hand, explicitly learns a model of the environment’s dynamics and leverages this model to facilitate policy optimization [Wang et al., 2019, Luo et al., 2024]. When the model possesses a certain structure (*e.g.*, linear quadratic regulators (LQRs)), it can be shown that optimal policies can be derived efficiently. However, in complex domains where the state transition can be nonlinear or non-deterministic, advanced modeling techniques (*e.g.*, recurrent [Hafner et al., 2019b,a], attentional [Chen et al., 2022a, Micheli et al., 2022], and diffusion-based models [Ding et al., 2024, Alonso et al., 2024]) with larger capacity become necessary in order to accurately reflect the true dynamics and reduce the approximation error. This introduces a dilemma analogous to that faced in model-free RL: with non-linear models, solving for an optimal policy via planning is computationally intractable, and becoming a long-standing challenging problem in control community [Khalil and Minor, 2015]. Consequently, practical model-based RL must resort to approximate inference methods, such as Dyna-style planning [Kurutach et al., 2018, Janner et al., 2019, Luo et al., 2024] or backpropagating the gradient through the models [Deisenroth and Rasmussen, 2011, Heess et al., 2015]. These compromises not only risk converging to suboptimal solutions, but also incur substantial costs both during training and inference due to their intricate designs, and thus waste the flexibility in modeling and effort in learning.

Spectral Representation Learning

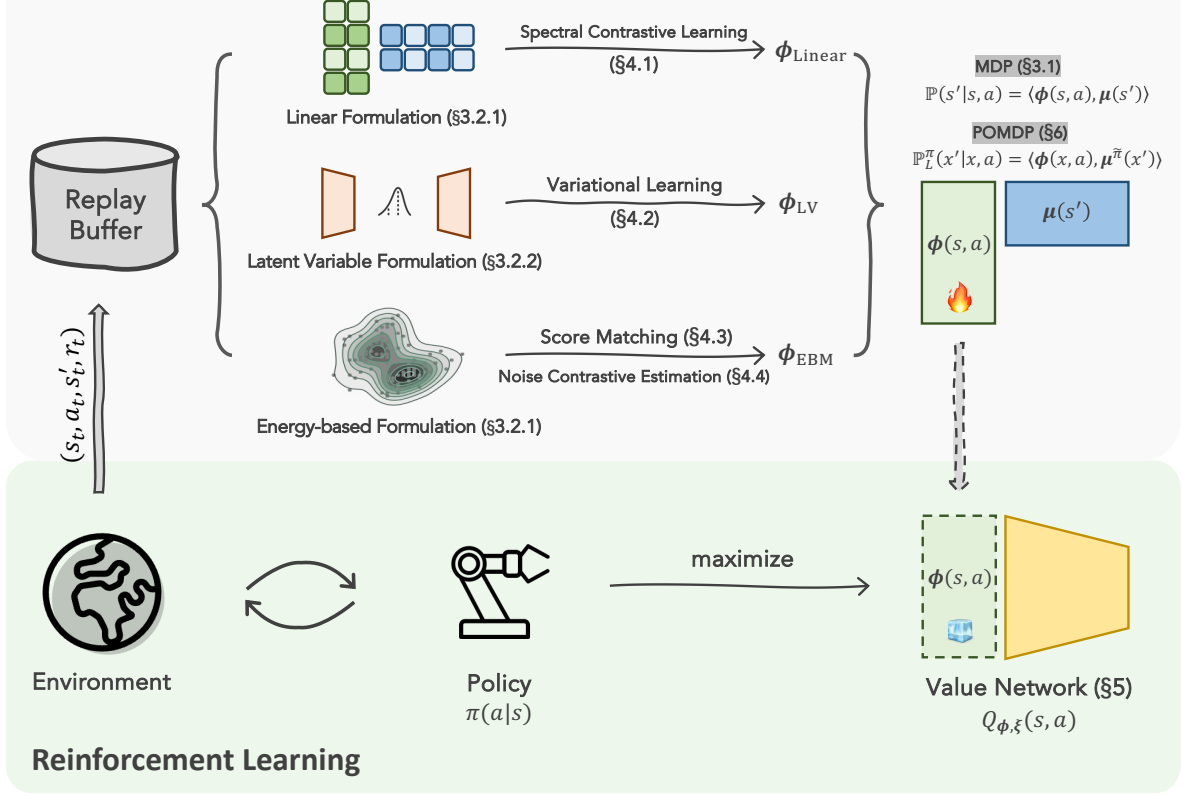


Figure 1: The overview of spectral representation-based reinforcement learning.

In conclusion, a persistent challenge pervades both model-based and model-free reinforcement learning: there is a lack of unified frameworks that can be simultaneously characterized by rigorous statistical guarantees and realized as computationally efficient, practical algorithms. This fundamental challenge leads to a very natural question:

Can we develop both provably efficient and practically effective algorithms for reinforcement learning?

Motivated by the recent success of representation learning, we present *spectral representations* as an affirmative answer to the above question. Specifically, spectral representations stem from the functional decomposition of the transition probability operator in MDP, thereby encoding sufficient information about the underlying dynamics. Leveraging an analysis analogous to the linear MDP literature [Jin et al., 2020], it can be demonstrated that the Q -value functions in RL can be sufficiently expressed with spectral representations, which paves the way for efficient learning and planning. Although several algorithms have been developed to leverage the power of spectral representations for reinforcement learning [Ren et al., 2022, Zhang et al., 2022, Ren et al., 2023a,b, Zhang et al., Shribak et al., 2024], this field nevertheless lacks a coherent framework to unify these methods, elucidate their connections, and conduct fair comparison. This survey aims to fill this blank by organizing these disparate methods into a cohesive overview and systematically

benchmarking them through controlled experiments.

We illustrate the structure of this survey in Figure 1. Specifically, after introducing the background knowledge in Section 2, Section 3 begins with a comprehensive overview of the spectral representation, covering its definitions and properties (Section 3.1) and its construction with different dynamics structures (Section 3.2). To address the intractability of spectral decomposition and maximum likelihood estimation (MLE) in large-scale spaces, Section 4 reviews practical algorithms for learning these representations directly from data. Next, Section 5 details how to integrate these learned representations into the reinforcement learning pipeline. Section 6 extends the framework to partially observable Markov decision processes (POMDPs), thereby accommodating more realistic decision-making scenarios. Finally, to validate the effectiveness as well as to facilitate further research in this direction, Section 7 presents an extensive empirical study. We release a unified codebase and benchmark performance on over 20 continuous control tasks from the DeepMind Control Suite [Tassa et al., 2018], encompassing diverse settings that include both fully observable state-based inputs and partially observable visual data. Generally, the algorithms based on spectral representations outperform their model-free counterparts, especially as task dynamics become more complex. In visual settings, these methods achieve performance comparable or superior to state-of-the-art model-based algorithms while obviating the need for computationally expensive trajectory synthesis. Finally, through a detailed ablation analysis, we investigate the influence of certain key design choices to provide a deeper understanding of these methods.

2 Preliminaries

We formulate the task as a Markov Decision Process (MDP) specified by a tuple $\mathcal{M} = \langle \mathcal{S}, \mathcal{A}, \mathbb{P}, r, \gamma, d_0 \rangle$, where \mathcal{S} is the state space, \mathcal{A} is the action space, $\mathbb{P} : \mathcal{S} \times \mathcal{A} \rightarrow \Delta(\mathcal{S})$ specifies the transition probability of states, $r : \mathcal{S} \times \mathcal{A} \rightarrow \mathbb{R}$ is the instantaneous reward function, $\gamma \in [0, 1)$ is the discounting factor and $d_0 \in \Delta(\mathcal{S})$ is the initial state distribution. The agents start with an initial state $s_0 \sim d_0$ and select an action $a_t \sim \pi(\cdot | s_t)$ following its policy $\pi : \mathcal{S} \rightarrow \Delta(\mathcal{A})$. The environment then takes a_t , transits to a new state s_{t+1} , and provides scalar feedback $r_t = r(s_t, a_t)$ to the agent. RL seeks to optimize the policy to maximize its expected cumulative return, defined as:

$$\mathcal{J}(\pi, \mathcal{M}) := \mathbb{E}_{a_t \sim \pi(\cdot | s_t), s_{t+1} \sim \mathbb{P}(\cdot | s_t, a_t)} \left[\sum_{t=0}^{\infty} \gamma^t r(s_t, a_t) \middle| s_0 \sim d_0 \right]. \quad (1)$$

To evaluate the values of each state and action, we define the state value functions $V^\pi : \mathcal{S} \rightarrow \mathbb{R}$ and state-action value functions $Q^\pi : \mathcal{S} \times \mathcal{A} \rightarrow \mathbb{R}$ of a given policy π as:

$$\begin{aligned} V^\pi(s) &:= \mathbb{E}_{a_t \sim \pi(\cdot | s_t), s_{t+1} \sim \mathbb{P}(\cdot | s_t, a_t)} \left[\sum_{t=0}^{\infty} \gamma^t r(s_t, a_t) \middle| s_0 = s \right], \\ Q^\pi(s, a) &:= \mathbb{E}_{a_t \sim \pi(\cdot | s_t), s_{t+1} \sim \mathbb{P}(\cdot | s_t, a_t)} \left[\sum_{t=0}^{\infty} \gamma^t r(s_t, a_t) \middle| s_0 = s, a_0 = a \right]. \end{aligned} \quad (2)$$

V^π and Q^π satisfy the following recursion:

$$\begin{aligned} Q^\pi(s, a) &= r(s, a) + \gamma \mathbb{E}_{s_{t+1} \sim \mathbb{P}(\cdot | s_t, a_t)} [V^\pi(s_{t+1})] \\ &= r(s, a) + \gamma \mathbb{E}_{s_{t+1} \sim \mathbb{P}(\cdot | s_t, a_t), a_{t+1} \sim \pi(\cdot | s_{t+1})} [Q^\pi(s_{t+1}, a_{t+1})], \end{aligned} \quad (3)$$

which is also known as the Bellman equation. With the help of value functions, the objective of RL can be conveniently defined as finding $\pi^* = \operatorname{argmax}_\pi \mathbb{E}_{s \sim d_0} [V^\pi(s)] = \operatorname{argmax}_\pi \mathbb{E}_{s \sim d_0, a \sim \pi} [Q^\pi(s, a)]$.

Finally, we define the *occupancy measure* $d^\pi(\cdot, \cdot) \in \Delta(\mathcal{S} \times \mathcal{A})$ as the normalized discounted probability of visiting (s, a) under policy π :

$$d^\pi(s, a) := (1 - \gamma) \mathbb{E}_{\pi, \mathbb{P}} \left[\sum_{t=0}^{\infty} \gamma^t \mathbb{I}\{s_t = s, a_t = a\} \right]. \quad (4)$$

Based on the stationary condition, the occupancy measure satisfies the following recursion:

$$d^\pi(s, a) = (1 - \gamma) d_0(s) \pi(a|s) + \gamma \int d^\pi(\tilde{s}, \tilde{a}) \mathbb{P}^\pi(s, a|\tilde{s}, \tilde{a}) d\tilde{s} d\tilde{a}, \quad (5)$$

where $\mathbb{P}^\pi(s, a|\tilde{s}, \tilde{a})$ is a shorthand for $\mathbb{P}(s|\tilde{s}, \tilde{a})\pi(a|s)$.

3 The Framework of Spectral Representations

This section introduces a spectral perspective on the transition dynamics of MDPs by formalizing them through a functional decomposition within a Hilbert space. Crucially, such linear structure inspires a family of representations, which we term *spectral representations*, that can capture the characteristics of the system dynamics and allow for sufficient expression of Q -value functions (Section 3.1). We then reveal how to construct these spectral representations for both linear and non-linear dynamics (Section 3.2), demonstrating the wide applicability of this framework.

3.1 Spectral View of MDPs

While seminal work in reinforcement learning has proposed efficient algorithms for tabular MDPs with finite state and action spaces [Auer et al., 2008, Dann and Brunskill, 2015, Agrawal and Jia, 2017], scaling to large or continuous spaces has remained a challenge. Recent works have turned to function approximations to overcome such challenges. A prominent approach in this direction is the linear (low-rank) MDP hypothesis [Jin et al., 2020], which posits that the transition operator admits a low-rank linear decomposition. Inspired by this, we consider a more generalized version without the finite rank assumption. Specifically, for any well-behaved transition operator \mathbb{P} and reward function r , there always exist two feature maps $\phi : \mathcal{S} \times \mathcal{A} \rightarrow \mathcal{H}$, $\mu : \mathcal{S} \rightarrow \mathcal{H}$ and a vector $\theta_r \in \mathcal{H}$ for some proper Hilbert space \mathcal{H} , such that for $\forall (s, a) \in \mathcal{S} \times \mathcal{A}$, we have

$$\begin{aligned} \mathbb{P}(s'|s, a) &= \langle \phi(s, a), \mu(s') \rangle_{\mathcal{H}}, \\ r(s, a) &= \langle \phi(s, a), \theta_r \rangle_{\mathcal{H}}. \end{aligned} \quad (6)$$

In fact, since the feature maps and the vector can be infinite-dimensional, such a decomposition always exists for the transition kernel \mathbb{P} . To see this, the singular value decomposition (SVD) of the transition operator [Mollenhauer et al., 2020] gives a concrete example:

$$\mathbb{P}(s'|s, a) = \sum_{i \in I} \sigma_i u_i(s, a) v_i(s'), \quad (7)$$

where I is an finite or countably infinite ordered index set, $\{u_i\}_{i \in I}$ and $\{v_i\}_{i \in I}$ are two orthogonal systems of the function spaces on $\mathcal{S} \times \mathcal{A}$ and \mathcal{S} , respectively. By expressing this summation as an

inner product, we obtain a realization of the aforementioned linear decomposition. Furthermore, commonly adopted structures in the literature are instantiations of the decomposition in (6) with additional assumptions. For example, linear MDP assumes $\mathcal{H} = \mathbb{R}^d$ for some finite d . Tabular MDP is also a special case, where $\mathcal{H} = \mathbb{R}^d$ with $d = |\mathcal{S}| \times |\mathcal{A}|$ and the feature map $\phi(s, a)$ is the canonical basis vector $e_{(s, a)} \in \mathbb{R}^d$.

A key consequence of this linear structure is that the Q -value functions of any given policy π also inherit this linearity [Yao et al., 2014, Jin et al., 2020, Yang and Wang, 2020].

Lemma 1 *For MDPs with (6) and any policy π , there exists weights $\eta^\pi \in \mathcal{H}$ such that $\forall (s, a) \in \mathcal{S} \times \mathcal{A}$, $Q^\pi(s, a) = \langle \phi(s, a), \eta^\pi \rangle_{\mathcal{H}}$.*

Proof The linearity of Q -value functions can be examined by the Bellman equation:

$$\begin{aligned} Q^\pi(s, a) &= r(s, a) + \gamma \int_{\mathcal{S}} \mathbb{P}(s'|s, a) V(s') ds' \\ &= \langle \phi(s, a), \theta_r \rangle_{\mathcal{H}} + \gamma \left\langle \phi(s, a), \int_{\mathcal{S}} \mu(s') V(s') ds' \right\rangle_{\mathcal{H}} \\ &= \left\langle \phi(s, a), \underbrace{\theta_r + \gamma \int_{\mathcal{S}} \mu(s') V(s') ds'}_{\eta^\pi} \right\rangle_{\mathcal{H}}. \end{aligned} \quad (8)$$

■

That is, Q -value functions lie in the linear function space spanned by the same feature map $\phi(s, a)$. This property is significant for two reasons. First, it simplifies theoretical analysis by allowing us to focus on linear Q -value functions, thereby reducing the complexity and facilitating uncertainty quantification. Second, it suggests that ϕ can serve as a representation for efficient algorithm design, as we can first extract ϕ from the dynamics and only learn the rest part (*i.e.*, η^π) with reinforcement learning. Given that $\phi(s, a)$ spans the same space as the orthogonal system from SVD, we term such representations as *spectral representations*.

Remark (Connection to Existing Representations from Decomposition View) To better situate the proposed spectral representations in the vast representation learning literature, we summarize existing representations that stem from spectral decomposition of transition-related matrices in Table 1. As discussed, spectral representations are derived from the left singular vectors of the single-step transition operator. In contrast, successor features [Dayan, 1993, Kulkarni et al., 2016, Barreto et al., 2017] are actually the left singular vector of $(I - \gamma \mathbb{P}^\pi)^{-1}$, as proved in [Ren et al., 2023b], which summarizes future state visitation from given states under a prefixed policy. The Laplacian-based methods [Wu et al., 2018] compute representations from the eigenvectors of the symmetrized transition matrix with the largest eigenvalues. Finally, if the reward function is known a priori, the Krylov basis [Petrick, 2007] suggests using the series $\{(\mathbb{P}^\pi)^i r\}_{i=1}^k$ as the representation for value functions.

Besides connecting the spectral representation to existing representations through the decomposition lens, more importantly, such a view also reveals the advantages of spectral representation over existing representation. Existing spectral representations are derived from \mathbb{P}^π (the policy-specific transition operator), which inherently introduces inter-state dependency tied to the specific policy π . This results in an unnecessary inductive bias in the state-only spectral features, potentially

Table 1: A unified matrix decomposition perspective of various representations. In this table, `svd` and `eig` denotes SVD and eigen decomposition, \mathbb{P}^π denotes the state transition $\mathbb{P}(s'|s)$ under policy π , and Λ is a diagonal matrix.

Representation	Decomposition
Spectral Representation	<code>svd</code> (\mathbb{P})
Successor Feature [Dayan, 1993]	<code>svd</code> $((I - \gamma \mathbb{P}^\pi)^{-1})$
Laplacian [Wu et al., 2018]	<code>eig</code> $(\Lambda \mathbb{P}^\pi + (\mathbb{P}^\pi)^\top \Lambda)$
Krylov Basis [Petrik, 2007]	$\{(\mathbb{P}^\pi)^i r\}_{i=1}^k$

hindering generalizability across different policies. Furthermore, these methods entirely neglect the exploration dilemma: the policy influences the data composition used for representation learning, yet the representations simultaneously affect policy optimization. This coupling significantly complicates the process. In contrast, the spectral representation investigated in this paper sidesteps the undesired dependency on π by extracting state-action representations from $\mathbb{P}(s'|s, a)$.

Remark (Primal-Dual Spectral Representations) With a fixed policy π , if we consider the spectral decomposition of the state-action transition kernel and the initial distribution:

$$\begin{aligned} d_0(s) &= \langle \boldsymbol{\theta}_d, \boldsymbol{\mu}(s) \rangle_{\mathcal{H}}, \\ \mathbb{P}^\pi(s', a'|s, a) &= \mathbb{P}(s'|s, a)\pi(a'|s') = \left\langle \boldsymbol{\phi}(s, a), \underbrace{\boldsymbol{\mu}(s')\pi(a'|s')}_{\boldsymbol{\mu}^\pi(s', a')} \right\rangle_{\mathcal{H}}, \end{aligned} \quad (9)$$

then, according to the recursion in (5), the occupancy measure also admits the linear structure over the other side of the factor $\boldsymbol{\mu}^\pi(s, a)$:

$$\begin{aligned} d^\pi(s, a) &= (1 - \gamma)d_0(s)\pi(a|s) + \gamma \int d^\pi(\tilde{s}, \tilde{a})\mathbb{P}^\pi(s, a|\tilde{s}, \tilde{a})d\tilde{s}d\tilde{a} \\ &= (1 - \gamma) \langle \boldsymbol{\theta}_d, \boldsymbol{\mu}^\pi(s, a) \rangle_{\mathcal{H}} + \gamma \int d^\pi(\tilde{s}, \tilde{a}) \langle \boldsymbol{\phi}(\tilde{s}, \tilde{a}), \boldsymbol{\mu}^\pi(s, a) \rangle_{\mathcal{H}} d\tilde{s}d\tilde{a} \\ &= \left\langle \underbrace{(1 - \gamma)\boldsymbol{\theta}_d + \gamma \int d^\pi(\tilde{s}, \tilde{a})\boldsymbol{\phi}(\tilde{s}, \tilde{a})d\tilde{a}}_{\boldsymbol{\eta}^\pi}, \boldsymbol{\mu}^\pi(s, a) \right\rangle_{\mathcal{H}}. \end{aligned} \quad (10)$$

Exploiting this structure, Hu et al. [2024] reduces the saddle-point optimization of the off-policy evaluation problem to a convex-concave objective, using $\boldsymbol{\phi}(s, a)$ as the primal representation for Q -value functions and $\boldsymbol{\mu}^\pi(s, a)$ as the dual representation for the occupancy measure.

3.2 Identifying Spectral Representations from Dynamics

However, although the decomposition (6) holds in general, the system dynamics do not necessarily admit this form. In this section, we will examine popular models of system dynamics and reveal how to derive their corresponding spectral representations. Our discussion begins with the most straightforward case of linear dynamics, and finally extends to complex non-linear dynamics, such

as latent-variable models and energy-based models. For the ease of presentation, we will only consider full-observable MDPs in this section.

3.2.1 Linear Formulation

Consider the case where the system dynamics is linear, *i.e.*, there exists $\varphi : \mathcal{S} \times \mathcal{A} \rightarrow \mathbb{R}^d$ and $\nu : \mathcal{S} \rightarrow \mathbb{R}^d$ such that

$$\mathbb{P}_{\text{Linear}}(s'|s, a) = \varphi(s, a)^\top \nu(s'), \quad (11)$$

By comparing this linear formulation (11) with (6), we instantly identify the spectral representation as $\phi(s, a) = \varphi(s, a) \in \mathbb{R}^d$. This is theoretically equivalent to the linear MDP hypothesis in [Jin et al. \[2020\]](#); however, we note that this structure is limited, as the finite-rank linearity assumption is strong and restricts the model’s expressive capacity.

3.2.2 Latent Variable Formulation

Consider a transition operator \mathbb{P}_{LV} with a latent variable structure. Assuming the latent variable is $z \in \mathcal{Z}$ and there exist two probability measures $\varphi(z|s, a)$ and $\nu(s'|z)$ such that the latent variable dynamics model can be expressed as

$$\mathbb{P}_{\text{LV}}(s'|s, a) = \int_{\mathcal{Z}} \varphi(z|s, a) \nu(s'|z) dz, \quad (12)$$

where $\varphi(\cdot|s, a) : \mathcal{S} \times \mathcal{A} \rightarrow \Delta(\mathcal{Z})$ and $\nu(\cdot|z) : \mathcal{Z} \rightarrow \Delta(\mathcal{S})$. Notably, if the measures $\varphi(\cdot|s, a) \in L_2$ and $\nu(s'|\cdot) \in L_2$, the integral in the latent variable formulation can also be formulated as an inner product [\[Ren et al., 2023a\]](#):

$$\mathbb{P}_{\text{LV}}(s'|s, a) = \langle \varphi(\cdot|s, a), \nu(s'|\cdot) \rangle_{L_2}, \quad (13)$$

which instantly follows the decomposition defined in (6) and recognizes the measure $\varphi(\cdot|s, a)$ as the spectral representation, denoted as ϕ_{LV} . The representation ϕ_{LV} can be finite or infinite dimensional for discrete or continuous latent variable z , respectively.

In fact, this structure is widely adopted in model-based reinforcement learning and world models with varied specific choices for the latent space and distributions. For instance, setting $\mathcal{Z} = \mathbb{R}^d$ and using Gaussian distributions for p recovers the dynamics modeling used in PlaNet [\[Hafner et al., 2019b\]](#) and Dreamer [\[Hafner et al., 2019a\]](#); while setting $Z = \{1, 2, \dots, D\}$ and $p(\cdot|s, a)$ as Categorical distributions recovers the models in DreamerV2 [\[Hafner et al., 2020\]](#) and DreamerV3 [\[Hafner et al., 2023\]](#). Moreover, such latent dynamics can also be built upon learned state representations, as demonstrated by [Zhou et al.](#) and [Xiang et al. \[2025\]](#).

Remark (Theoretical limitations of ϕ_{LV}). Since $\varphi(\cdot|s, a)$ must be a valid probability measure, latent variable models are thus limited in expressiveness as compared to the unconstrained version. In fact, [Agarwal et al. \[2020\]](#) has demonstrated that the simplex feature ϕ_{LV} can be exponentially weaker than the linear counterpart ϕ_{Linear} , meaning that ϕ_{LV} may require exponentially more dimensions than ϕ_{Linear} to characterize the same transition operator. However, as the theoretical characterization in Section 5 suggests, the apparent dimension may not be a good measure of the complexity of the representations. As long as the transition operator satisfies some regularity conditions, sampling-efficient learning is still possible.

3.2.3 Energy-based Formulation

As one of the most flexible model parameterizations, energy-based models (EBMs) associate the transition probability with an energy function $E(s, a, s')$:

$$\mathbb{P}_{\text{EBM}}(s'|s, a) = \frac{\exp(E(s, a, s'))}{Z(s, a)} = \frac{\exp(\boldsymbol{\varphi}(s, a)^\top \boldsymbol{\nu}(s'))}{Z(s, a)}, \quad (14)$$

where the $Z(s, a)$ is the normalizing factor satisfying $Z(s, a) = \int_{\mathcal{S}} \exp(E(s, a, s')) ds'$, and the energy function can be factorized as the inner product of $\boldsymbol{\varphi} : \mathcal{S} \times \mathcal{A} \rightarrow \mathbb{R}^d$ and $\boldsymbol{\nu} : \mathcal{S} \rightarrow \mathbb{R}^d$. By simple algebra manipulation,

$$\boldsymbol{\varphi}(s, a)^\top \boldsymbol{\nu}(s') = -\frac{1}{2} (\|\boldsymbol{\varphi}(s, a) - \boldsymbol{\nu}(s')\|^2 - \|\boldsymbol{\varphi}(s, a)\|^2 - \|\boldsymbol{\nu}(s')\|^2), \quad (15)$$

and therefore,

$$\mathbb{P}_{\text{EBM}}(s'|s, a) = \frac{\exp(\frac{1}{2}\|\boldsymbol{\varphi}(s, a)\|^2) \exp(-\frac{1}{2}\|\boldsymbol{\varphi}(s, a) - \boldsymbol{\nu}(s')\|^2) \exp(\frac{1}{2}\|\boldsymbol{\nu}(s')\|^2)}{Z(s, a)}. \quad (16)$$

In order to reveal the linear perspective of (16), note that $\exp(\frac{1}{2}\|\boldsymbol{\varphi}(s, a) - \boldsymbol{\nu}(s')\|)$ in (16) is precisely a Gaussian kernel, and therefore

$$\begin{aligned} \mathbb{P}_{\text{EBM}}(s'|s, a) &= \frac{\exp(\frac{1}{2}\|\boldsymbol{\varphi}(s, a)\|^2) k(\boldsymbol{\varphi}(s, a), \boldsymbol{\nu}(s')) \exp(\frac{1}{2}\|\boldsymbol{\nu}(s')\|^2)}{Z(s, a)} \\ &= \left\langle \frac{\exp(\frac{1}{2}\|\boldsymbol{\varphi}(s, a)\|^2)}{Z(s, a)} k(\boldsymbol{\varphi}(s, a), \cdot), k(\cdot, \boldsymbol{\nu}(s')) \exp(\frac{1}{2}\|\boldsymbol{\nu}(s')\|^2) \right\rangle_{\mathcal{H}_k}. \end{aligned} \quad (17)$$

This final expression represents the transition as an inner product in \mathcal{H}_k , the reproducing kernel Hilbert space of the Gaussian kernel k , and satisfies the decomposition in (6). However, this RKHS representation $k(\boldsymbol{\varphi}(s, a), \cdot)$ and $k(\cdot, \boldsymbol{\nu}(s'))$ is conceptual and implicit. To derive a concrete representation, [Ren et al. \[2022\]](#) and [Shribak et al. \[2024\]](#) adopt random Fourier features [\[Rahimi and Recht, 2007\]](#), as defined in the following lemma.

Lemma 2 *(Random Fourier features [Rahimi and Recht, 2007]) Consider a shift invariant kernel $k(\mathbf{x}, \mathbf{y}) = k(\mathbf{x} - \mathbf{y})$ on \mathbb{R}^d . Define $\zeta_{\boldsymbol{\omega}}(\mathbf{x}) = e^{j\boldsymbol{\omega}^\top \mathbf{x}}$, we have*

$$k(\mathbf{x} - \mathbf{y}) = \int_{\mathbb{R}^d} p(\boldsymbol{\omega}) e^{j\boldsymbol{\omega}^\top (\mathbf{x} - \mathbf{y})} d\boldsymbol{\omega} = \mathbb{E}_{\boldsymbol{\omega} \sim p(\boldsymbol{\omega})} [\zeta_{\boldsymbol{\omega}}(\mathbf{x}) \zeta_{\boldsymbol{\omega}}(\mathbf{y})^*], \quad (18)$$

where $p(\boldsymbol{\omega})$ is the Fourier transform of the kernel $k(\Delta)$. Particularly, for $k(\Delta) = \exp(-\frac{\|\Delta\|_2^2}{2})$, then $p(\boldsymbol{\omega}) = (2\pi)^{-\frac{d}{2}} \exp(-\frac{\|\boldsymbol{\omega}\|_2^2}{2})$.

The expectation in (18) can be further approximated with Monte-Carlo samples of $\{\boldsymbol{\omega}_i\}_{i=1}^N \sim p(\boldsymbol{\omega})$. Besides, since we are working with real-valued transition probabilities, we can replace $\zeta_{\boldsymbol{\omega}}(\mathbf{x})$

with $[\cos(\boldsymbol{\omega}^\top \mathbf{x}), \sin(\boldsymbol{\omega}^\top \mathbf{x})]^\top$. This leads to the final approximation of $k(\mathbf{x}, \mathbf{y})$:

$$\begin{aligned}
k(\mathbf{x} - \mathbf{y}) &= \mathbb{E}_{\boldsymbol{\omega} \sim p(\boldsymbol{\omega})} [\zeta_{\boldsymbol{\omega}}(\mathbf{x}) \zeta_{\boldsymbol{\omega}}(\mathbf{y})^*] \\
&\approx \begin{pmatrix} \frac{1}{\sqrt{N}} \cos(\boldsymbol{\omega}_1^\top \mathbf{x}) \\ \frac{1}{\sqrt{N}} \sin(\boldsymbol{\omega}_1^\top \mathbf{x}) \\ \vdots \\ \frac{1}{\sqrt{N}} \cos(\boldsymbol{\omega}_N^\top \mathbf{x}) \\ \frac{1}{\sqrt{N}} \sin(\boldsymbol{\omega}_N^\top \mathbf{x}) \end{pmatrix}^\top \begin{pmatrix} \frac{1}{\sqrt{N}} \cos(\boldsymbol{\omega}_1^\top \mathbf{y}) \\ \frac{1}{\sqrt{N}} \sin(\boldsymbol{\omega}_1^\top \mathbf{y}) \\ \vdots \\ \frac{1}{\sqrt{N}} \cos(\boldsymbol{\omega}_N^\top \mathbf{y}) \\ \frac{1}{\sqrt{N}} \sin(\boldsymbol{\omega}_N^\top \mathbf{y}) \end{pmatrix} \\
&= \langle \zeta_N(\mathbf{x}), \zeta_N(\mathbf{y}) \rangle_{L_2},
\end{aligned} \tag{19}$$

where we use $\zeta_N(\mathbf{x})$ to denote the $2N$ -dimensional sinusoidal vector inside the expectation and the frequencies $\{\boldsymbol{\omega}_i\}_{i=1}^N$ are sampled i.i.d. from $p(\boldsymbol{\omega})$.

Applying this to the Gaussian kernel $\exp(-\frac{1}{2}\|\boldsymbol{\varphi}(s, a) - \boldsymbol{\nu}(s')\|^2)$, we have

$$\begin{aligned}
\mathbb{P}_{\text{EBM}}^*(s' | s, a) &= \frac{\exp(\|\boldsymbol{\varphi}(s, a)\|^2) \exp(-\frac{1}{2}\|\boldsymbol{\varphi}(s, a) - \boldsymbol{\nu}(s')\|^2) \exp(\|\boldsymbol{\nu}(s')\|^2)}{Z(s, a)} \\
&= \underbrace{\left\langle \frac{\exp(\|\boldsymbol{\varphi}(s, a)\|^2)}{Z(s, a)} \zeta_N(\boldsymbol{\varphi}(s, a)), \underbrace{\exp(\|\boldsymbol{\nu}(s')\|^2) \zeta_N(\boldsymbol{\nu}(s'))}_{\boldsymbol{\mu}_{\text{EBM}}(s')} \right\rangle}_{\phi_{\text{EBM}}(s, a)},
\end{aligned} \tag{20}$$

That is, we can obtain linear factorization for transition operators parameterized as factorized EBMs, and the corresponding spectral representation is denoted $\phi_{\text{EBM}}^*(s, a)$.

As an ending note, we can continue to demonstrate that the normalizing factor $Z(s, a)$ can also be expressed by $\boldsymbol{\varphi}(s, a)$, such that the EBM spectral representation ϕ_{EBM} depends exclusively on the factorized energy $\boldsymbol{\varphi}$ and random Fourier frequencies. This can be examined by

$$\begin{aligned}
Z(s, a) &= \int_{\mathcal{S}} \left\langle \exp(\|\boldsymbol{\varphi}(s, a)\|^2) \zeta_N(\boldsymbol{\varphi}(s, a)), \boldsymbol{\mu}_{\text{EBM}}(s') \right\rangle ds' \\
&= \left\langle \exp(\|\boldsymbol{\varphi}(s, a)\|^2) \zeta_N(\boldsymbol{\varphi}(s, a)), \underbrace{\int_{\mathcal{S}} \boldsymbol{\mu}_{\text{EBM}}(s') ds'}_{\mathbf{u}} \right\rangle.
\end{aligned} \tag{21}$$

Therefore, we have

$$\begin{aligned}
\phi_{\text{EBM}}(s, a) &= \frac{\exp(\|\boldsymbol{\varphi}(s, a)\|^2) \zeta_N(\boldsymbol{\varphi}(s, a))}{\langle \exp(\|\boldsymbol{\varphi}(s, a)\|^2) \zeta_N(\boldsymbol{\varphi}(s, a)), \mathbf{u} \rangle} \\
&= \frac{\zeta_N(\boldsymbol{\varphi}(s, a))}{\langle \zeta_N(\boldsymbol{\varphi}(s, a)), \mathbf{u} \rangle}, \quad \text{where } \mathbf{u} \in \mathbb{R}^{2N}.
\end{aligned} \tag{22}$$

Remark. The case of stochastic nonlinear control [Zheng et al., 2022, Ren et al., 2022, 2025, Ma et al., 2025], whose state-space dynamics follows the form $s' = \boldsymbol{\varphi}(s, a) + v$ where v is a Gaussian noise $\mathcal{N}(0, \sigma^2 I)$, can be understood as a special instance of either the energy-based formulation or latent-variable formulation. In this case, the state transition dynamics can be written as $\mathbb{P}(s' | s, a) \propto \exp\left(-\frac{\|s' - \boldsymbol{\varphi}(s, a)\|^2}{2\sigma^2}\right)$. By applying the same random Fourier features, we can recover the spectral

structure analogous to (22). Alternatively, the connection to the latent-variable formulation can be seen through the decomposition:

$$\mathbb{P}(s'|s, a) = \frac{1}{\sqrt{2\pi}\sigma} \exp\left(-\frac{\|s' - \varphi(s, a)\|^2}{2\sigma^2}\right) = \langle p(\cdot|s, a), p(s'|\cdot) \rangle_{L_2}, \quad (23)$$

where $p(z|s, a) \propto \exp(-\|z - \varphi(s, a)\|^2/\sigma^2)$ and $p(s'|z) \propto \exp(-\|z - s'\|^2/\sigma^2)$. Our formulations offer greater flexibility by conducting the modeling in the latent space and by generalizing the latent distributions beyond Gaussian distributions, respectively.

4 Algorithms for Learning Spectral Representations

In Section 3, we studied how spectral representations can be extracted from transition operators with different structures, using either a linear formulation ϕ_{Linear} , a latent variable formulation ϕ_{LV} , or an energy-based formulation ϕ_{EBM} . We will discuss the corresponding learning methods for each parametrization from different perspectives.

We begin by estimating the representation ϕ_{Linear} in the context of linear formulation (11). Several works on linear MDPs [Agarwal et al., 2020, Uehara et al., 2021] derive the representation by solving the following maximum log-likelihood estimation (MLE) problem:

$$\begin{aligned} \max_{\phi, \mu} \quad & \mathbb{E}_{(s, a) \sim \rho, s' \sim \mathbb{P}(\cdot|s, a)} [\log \langle \phi(s, a), \mu(s') \rangle] \\ \text{s.t. } & \forall (s, a), \quad \int_S \langle \phi(s, a), \mu(s') \rangle ds' = 1, \end{aligned} \quad (24)$$

which, however, is notoriously difficult for a large or continuous state space, since enforcing or even just computing the constraint requires an integral over the whole state space. To sidestep this burden, we review tractable alternatives to derive the representations in this section.

4.1 Representations from Spectral Contrastive Learning

With a slight abuse of notation, let $\mathbb{P}(s, a, s')$ denote the joint distribution of a state-action pair and its successor state, and let $\mathbb{P}(s, a)$ and $\mathbb{P}(s')$ be the corresponding marginals. A straightforward approach is to parameterize the conditional density $\mathbb{P}(s'|s, a) = \varphi_\theta(s, a)^\top \nu_\theta(s')$ with parameters θ and minimize the point-wise squared error:

$$\min_{\theta} \int_{\mathcal{S} \times \mathcal{A}} \int_{\mathcal{S}} \left\| \mathbb{P}(s'|s, a) - \varphi_\theta(s, a)^\top \nu_\theta(s') \right\|^2 ds da ds'. \quad (25)$$

Apparently, the triple integral over spaces makes it an intractable objective. Instead, **Speder** [Ren et al., 2023b] considers a parameterization modulated by a scaling factor $\mathbb{P}(s')$:

$$\mathbb{P}(s'|s, a) = \varphi_\theta(s, a)^\top (\mathbb{P}(s') \nu_\theta(s')). \quad (26)$$

As shown later, as long as $\mathbb{P}(s')$ is amenable to sampling, introducing this factor leads to a tractable optimization objective without altering the final representation. To train φ_θ and ν_θ , **Speder** leverages spectral contrastive learning [HaoChen et al., 2021, Ren et al., 2023b] to match a rebalanced

version of (26):

$$\begin{aligned}
\min_{\theta} \ell_{\text{SCL}}(\theta) &= \int_{\mathcal{S} \times \mathcal{A}} \int_{\mathcal{S}} \left\| \frac{\mathbb{P}(s, a, s')}{\sqrt{\lambda \mathbb{P}(s, a) \mathbb{P}(s')}} - \sqrt{\lambda \mathbb{P}(s, a) \mathbb{P}(s')} \boldsymbol{\varphi}_{\theta}(s, a)^{\top} \boldsymbol{\nu}_{\theta}(s') \right\|^2 ds da ds' \\
&= \lambda \mathbb{E}_{\mathbb{P}(s, a) \mathbb{P}(s')} \left[\left(\boldsymbol{\varphi}_{\theta}(s, a)^{\top} \boldsymbol{\nu}_{\theta}(s') \right)^2 \right] - 2 \mathbb{E}_{\mathbb{P}(s, a, s')} \left[\boldsymbol{\varphi}_{\theta}(s, a)^{\top} \boldsymbol{\nu}_{\theta}(s') \right] \\
&\quad + \underbrace{\int_{\mathcal{S} \times \mathcal{A}} \int_{\mathcal{S}} \left\| \frac{\mathbb{P}(s, a, s')}{\sqrt{\lambda \mathbb{P}(s, a) \mathbb{P}(s')}} \right\|^2 ds da ds'}_{\text{Const}}
\end{aligned} \tag{27}$$

This yields a practical contrastive learning-style objective that is compatible with stochastic gradient descent. Specifically, we can approximate the expectations in the objective by drawing samples from the empirical distributions (i.e., the replay buffer). For each state-action pair (s, a) drawn uniformly from the buffer, the ground-truth successor state serves as the positive sample s'_+ , and states randomly sampled from the buffer act as negative samples s'_- , thereby implementing the spectral contrastive loss as:

$$\min_{\theta} \ell_{\text{SCL}}(\theta) = \frac{\lambda}{N} \sum_{n=1}^N \left(\boldsymbol{\varphi}_{\theta}(s_n, a_n)^{\top} \boldsymbol{\nu}_{\theta}(s'_{n,-}) \right)^2 - \frac{2}{N} \sum_{n=1}^N \left(\boldsymbol{\varphi}_{\theta}(s_n, a_n)^{\top} \boldsymbol{\nu}_{\theta}(s'_{n,+}) \right) + \text{Const.} \tag{28}$$

Finally, the spectral representation can be recovered by $\boldsymbol{\phi}_{\text{Linear}} \approx \boldsymbol{\varphi}_{\theta^*}$. It must be noted that since in practice we must settle for a finite-dimensional representation $\boldsymbol{\varphi}_{\theta^*}$, such representations have limited expressive power for both transition probabilities and Q -value functions.

Remark (Singular Value Decomposition): Another alternative interpretation of (27) is that it is equivalent to the SVD of a scaled transition operator. Define $L_2(\mathcal{S} \times \mathcal{A})$ and $L_2(\mathcal{S})$ be the spaces of square summable functions over $\mathcal{S} \times \mathcal{A}$ and \mathcal{S} respectively, we consider the scaled transition kernel $\tilde{\mathcal{T}} : L_2(\mathcal{S} \times \mathcal{A}) \rightarrow L_2(\mathcal{S})$ which satisfies $(\tilde{\mathcal{T}}f)(s') = \int \frac{\mathbb{P}(s, a, s')}{\sqrt{\mathbb{P}(s, a) \mathbb{P}(s')}} f(s, a) d(s, a)$. Its SVD tries to find orthogonal eigen-functions $\boldsymbol{\varphi} = \{\boldsymbol{\varphi}_i\}_{i=1}^I$ to capture the principal components:

$$\begin{aligned}
&\max_{\boldsymbol{\varphi}_i^{\top} \boldsymbol{\varphi}_j = \mathbf{1}_{i=j}} \sum_{i=1}^I \left\| \int \frac{\mathbb{P}(s, a, s')}{\sqrt{\mathbb{P}(s, a) \mathbb{P}(s')}} \boldsymbol{\varphi}_i(s, a) d(s, a) \right\|_2^2 \\
&= \max_{\boldsymbol{\varphi}_i^{\top} \boldsymbol{\varphi}_j = \mathbf{1}_{i=j}} \max_{\nu_1, \dots, \nu_I} \sum_{i=1}^I \left(2 \iint \frac{\mathbb{P}(s, a, s')}{\sqrt{\mathbb{P}(s, a) \mathbb{P}(s')}} \boldsymbol{\varphi}_i(s, a) \nu_i(s, a) d(s, a) ds' - \int \nu_i(s')^2 ds' \right) \\
&= \max_{\mathbb{E}_{\mathbb{P}(s, a)} [\boldsymbol{\varphi}_i' \boldsymbol{\varphi}_j'] = \mathbf{1}_{i=j}} \max_{\nu_1', \dots, \nu_I'} \sum_{i=1}^I \left(2 \iint \mathbb{P}(s, a, s') \boldsymbol{\varphi}_i'(s, a) \nu_i'(s, a) d(s, a) ds' - \int \mathbb{P}(s') \nu_i'(s')^2 ds' \right) \\
&= \max_{\mathbb{E}_{\mathbb{P}(s, a)} [\boldsymbol{\varphi}_i' \boldsymbol{\varphi}_j'] = \mathbf{1}_{i=j}} \max_{\nu_1', \dots, \nu_I'} 2 \mathbb{E}_{\mathbb{P}(s, a, s')} \left[\sum_{i=1}^I \boldsymbol{\varphi}_i'(s, a) \nu_i'(s') \right] - \mathbb{E}_{\mathbb{P}(s, a) \mathbb{P}(s')} \left[\left(\sum_{i=1}^I \boldsymbol{\varphi}_i'(s, a) \nu_i'(s') \right)^2 \right]
\end{aligned} \tag{29}$$

where the first equality follows from the Fenchel duality of $\|\cdot\|_2^2$, the second equality comes from the change of variable $\boldsymbol{\varphi}_i'(s, a) = \frac{\boldsymbol{\varphi}_i(s, a)}{\sqrt{\mathbb{P}(s, a)}}$ and $\nu_i'(s') = \frac{\nu_i(s')}{\sqrt{\mathbb{P}(s')}}$, and the last equality is due to the

orthogonality constraint $\mathbb{E}[\varphi_i(s, a)\varphi_j(s, a)] = \mathbf{1}_{i=j}$:

$$\begin{aligned}
\mathbb{E}_{\mathbb{P}(s, a)\mathbb{P}(s')} \left[\left(\sum_{i=1}^I \varphi'_i(s, a)\nu'_i(s') \right)^2 \right] &= \mathbb{E}_{\mathbb{P}(s, a)\mathbb{P}(s')} \left[\sum_{i=1}^I (\varphi'_i(s, a)\nu'_i(s'))^2 \right] \\
&= \mathbb{E}_{\mathbb{P}(s')} \left[\sum_{i=1}^I (\nu'_i(s')\mathbb{E}_{\mathbb{P}(s, a)}[\varphi'_i(s, a)\varphi'_i(s, a)]\nu'_i(s')) \right] \\
&= \mathbb{E}_{\mathbb{P}(s')} \left[\sum_{i=1}^I \nu'_i(s')^2 \right].
\end{aligned} \tag{30}$$

Recognizing the summation in (29) as the inner product between the representations, the spectral contrastive loss in (27) is precisely the variational objective for an SVD of the scaled transition kernel, without the orthonormal constraint. Therefore, spectral contrastive loss (27) recovers the same subspace of SVD.

4.2 Representations from Variational Learning

When the transition operator possesses the latent variable structure as described in Section 3.2.2, **LV-Rep** [Ren et al., 2023a] employs variational learning to obtain a tractable surrogate objective of the original MLE (24). Specifically, suppose the transition operator is parameterized as $\mathbb{P}(s'|s, a) = \int \varphi_\theta(z|s, a)\nu_\theta(s'|z)dz$ for some valid probability measure $\varphi_\theta : \mathcal{S} \times \mathcal{A} \rightarrow \Delta(\mathcal{Z})$, then it follows from Jensen's inequality that

$$\begin{aligned}
\log \mathbb{P}(s'|s, a) &= \log \int \varphi_\theta(z|s, a)\nu_\theta(s'|z)dz = \log \int q_\theta(z|s, a, s') \frac{\varphi_\theta(z|s, a)\nu_\theta(s'|z)}{q_\theta(z|s, a, s')} dz \\
&\geq \underbrace{\mathbb{E}_{z \sim q_\theta(\cdot|s, a, s')} [\log \nu_\theta(s'|z)] - D_{\text{KL}}(q_\theta(\cdot|s, a, s') \parallel \varphi_\theta(\cdot|s, a))}_{\ell_{\text{ELBO}}(\theta)},
\end{aligned} \tag{31}$$

where $q_\theta(\cdot|s, a, s')$ is the variational distribution also parameterized by θ , and the RHS of the last inequality is also known as the evidence lower bound (ELBO) [Kingma and Welling, 2013]. We can also introduce a hyper-parameter $\beta \geq 0$ and optimize the β -VAE objective [Higgins et al., 2017] to balance the KL regularization term and the reconstruction term:

$$\ell_{\text{ELBO}, \beta}(\theta) = \mathbb{E}_{z \sim q_\theta(\cdot|s, a, s')} [\log \nu_\theta(s'|z)] - \beta D_{\text{KL}}(q_\theta(\cdot|s, a, s') \parallel \varphi_\theta(\cdot|s, a)). \tag{32}$$

Similarly, with the optimal parameter θ^* obtained by maximizing $\ell_{\text{ELBO}, \beta}$, the spectral representation ϕ_{LV} can be set as $\varphi_{\theta^*}(\cdot|s, a)$ based on (13).

4.3 Representations from Score Matching

In section 3.2.3, we described how to construct spectral representations ϕ_{EBM} from a factorized energy function $\varphi(s, a)^\top \nu(s')$. A key challenge with this is that estimating the energy function of EBMs with MLE requires computing the normalization factor, which is often intractable [LeCun et al., 2006, Song and Kingma, 2021]. Diffusion models [Ho et al., 2020, Song et al.] offer a promising solution for sampling from EBMs by estimating the *score functions* instead of the energy functions,

thereby bypassing the need for this normalization factor. Inspired by this, **Diff-SR** [Shribak et al., 2024] derives a tractable, score-based optimization objective for learning $\phi(s, a)$.

For a given state-action pair (s, a) , **Diff-SR** perturbs the samples from the ground-truth transition $s' \sim \mathbb{P}(s'|s, a)$ using a Gaussian kernel with a noise level chosen from a pre-defined schedule $\{\beta_m\}_{m=1}^M$. For a given noise level β , the perturbation kernel $\mathbb{P}(\tilde{s}'|s'; \beta)$ and the perturbed transition $\mathbb{P}(\tilde{s}'|s, a; \beta)$ are defined as:

$$\begin{aligned}\mathbb{P}(\tilde{s}'|s'; \beta) &= \mathcal{N}(\sqrt{1-\beta}s', \beta I), \\ \mathbb{P}(\tilde{s}'|s, a; \beta) &= \int_{\mathcal{S}} \mathbb{P}(s'|s, a) \mathbb{P}(\tilde{s}'|s'; \beta) ds'.\end{aligned}\quad (33)$$

where $\mathbb{P}(\tilde{s}'|s, a; \beta) \rightarrow \mathbb{P}(s'|s, a)$ as $\beta \rightarrow 0$. Following the EBM formulation, **Diff-SR** parameterizes this perturbed transition with θ :

$$\mathbb{P}(\tilde{s}|s, a; \beta) \propto \exp(\boldsymbol{\varphi}_\theta(s, a)^\top \boldsymbol{\nu}_\theta(\tilde{s}'; \beta)), \quad (34)$$

where $\boldsymbol{\varphi}_\theta : \mathcal{S} \times \mathcal{A} \rightarrow \mathbb{R}^d$ is shared across all noise levels. To learn $\boldsymbol{\varphi}_\theta$, **Diff-SR** matches the score function of the parameterized distribution $\nabla_{\tilde{s}'} \log \mathbb{P}(\tilde{s}'|s, a; \beta) \approx \boldsymbol{\varphi}_\theta(s, a)^\top \nabla_{\tilde{s}'} \boldsymbol{\nu}_\theta(\tilde{s}'; \beta)$ with that of the ground-truth corrupted transition, which yields the following score matching objective:

$$\ell_{\text{SM}}(\theta) = \mathbb{E}_{(s, a) \sim \rho, \tilde{s}' \sim \mathbb{P}(\cdot|s, a; \beta)} \left[\left\| \boldsymbol{\varphi}_\theta(s, a)^\top \nabla_{\tilde{s}'} \boldsymbol{\nu}_\theta(\tilde{s}'; \beta) - \nabla_{\tilde{s}'} \log \mathbb{P}(\tilde{s}'|s, a; \beta) \right\|^2 \right], \quad (35)$$

However, the ground-truth score remains intractable, as it involves integrating over all possible next states s' . To address this, **Diff-SR** uses the conditional score matching objective:

$$\ell_{\text{CSM}}(\theta) = \mathbb{E}_{(s, a) \sim \rho, s' \sim \mathbb{P}(\cdot|s, a), \tilde{s}' \sim \mathbb{P}(\cdot|s'; \beta)} \left[\left\| \boldsymbol{\varphi}_\theta(s, a)^\top \nabla_{\tilde{s}'} \boldsymbol{\nu}_\theta(\tilde{s}'; \beta) - \nabla_{\tilde{s}'} \log \mathbb{P}(\tilde{s}'|s'; \beta) \right\|^2 \right], \quad (36)$$

which shares the same optimal solution to ℓ_{SM} , as proved in the Appendix A of Shribak et al. [2024]. Note that the regression target has analytical forms when the perturbation kernel is known, and in our case, $\nabla_{\tilde{s}'} \log \mathbb{P}(\tilde{s}'|s'; \beta) = -(\tilde{s}' - \sqrt{1-\beta}s')/\beta$. In practice, **Diff-SR** directly parameterizes $\nabla_{\tilde{s}'} \boldsymbol{\nu}_\theta(\tilde{s}'; \beta)$ as a neural network $\boldsymbol{\kappa}_\theta : \mathbb{R}^{\text{dim}(\mathcal{S})} \times \mathbb{R} \rightarrow \mathbb{R}^{d \times \text{dim}(\mathcal{S})}$ and thereby avoids the need to compute second-order gradients.

After training is completed, spectral representations ϕ_{EBM} can be obtained according to $\phi_{\text{EBM}} \approx \frac{\zeta_N(\boldsymbol{\varphi}_{\theta^*}(s, a))}{\langle \zeta_N(\boldsymbol{\varphi}_{\theta^*}(s, a)), \mathbf{u} \rangle}$ (22), where \mathbf{u} will be specified later in section 5.

4.4 Representations from Noise Contrastive Estimation

Another effective approach to learning the energy function is noise contrastive estimation (NCE) [Ma and Collins, 2018, Gutmann and Hyvärinen, 2010, 2012]. Specifically, let $\tilde{\mathbb{P}}(s')$ be an arbitrary noise distribution, and we model the target density as:

$$\mathbb{P}(s'|s, a) \propto \tilde{\mathbb{P}}(s') \exp \left(\boldsymbol{\varphi}_\theta(s, a)^\top \boldsymbol{\nu}_\theta(s') \right). \quad (37)$$

For each state-action pair (s_n, a_n) , we draw one positive sample $s'_{n,0} \sim \mathbb{P}(s'|s, a)$ and K negative samples $\{s'_{n,k}\}_{k=1}^K$ i.i.d. from the noise distribution $\tilde{\mathbb{P}}(s')$. The *ranking-based NCE* tries to identify the positive sample among the negatives:

$$\ell_{\text{R-NCE}}(\theta) = \frac{1}{N} \sum_{n=1}^N \frac{\exp(\boldsymbol{\varphi}_\theta(s_n, a_n)^\top \boldsymbol{\nu}_\theta(s'_{n,0}))}{\sum_{k=1}^K \exp(\boldsymbol{\varphi}_\theta(s_n, a_n)^\top \boldsymbol{\nu}_\theta(s'_{n,k}))} \quad (38)$$

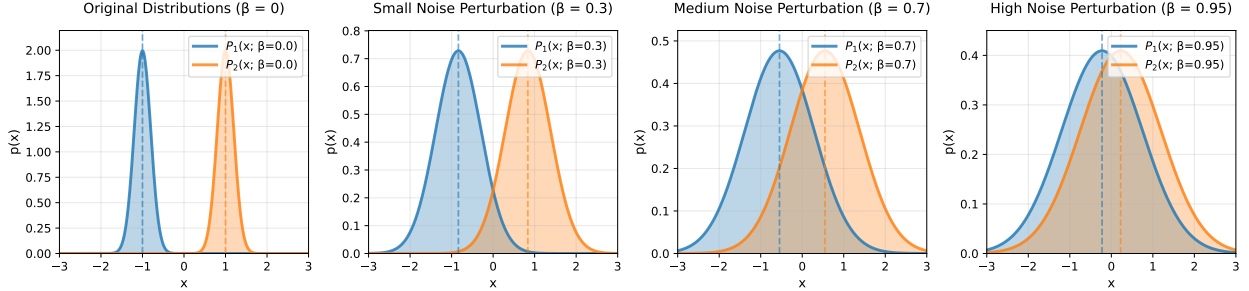


Figure 2: Illustrations of two nearly disjoint Gaussian distributions and their perturbed versions under various configurations of β . As β progresses from 0 to 1, they overlap with each other and it becomes increasingly difficult for NCE to tell the difference between these distributions.

The optimal parameter $\theta^* = \operatorname{argmin}_\theta \ell_{\text{R-NCE}}(\theta)$ provides an estimate of the energy function (37), combined with the negative distribution. Note that the noise distribution $\tilde{\mathbb{P}}(s')$ in (37) does not affect the extracted spectral representation ϕ_{EBM} , as it depends only on s' and can be absorbed into the other spectral component, μ_{EBM} .

However, when the negative sample distribution $\tilde{\mathbb{P}}(s')$ is trivial or disjoint from the true conditional density $\mathbb{P}(s'|s, a)$, NCE may yield poor representation since classifying between the positives and the negatives is too easy [Robinson et al., 2020, Rhodes et al., 2020]. While existing methods often address this by using more negative samples [Radford et al., 2021, Chen et al., 2022b] or designing more sophisticated noise distributions [Finn et al., 2016], we propose a simple solution inspired by diffusion models.

Specifically, we conduct NCE across different perturbed negative distributions $\tilde{\mathbb{P}}(\tilde{s}'; \beta)$ and perturbed EBMs $\mathbb{P}(\tilde{s}'|s, a; \beta)$, each of which is associated with a noise level β from the pre-defined schedule $\{\beta_m\}_{m=1}^M$:

$$\begin{aligned} \tilde{\mathbb{P}}(\tilde{s}'; \beta) &= \int_{\mathcal{S}} \mathbb{P}(\tilde{s}'|s'; \beta) \tilde{\mathbb{P}}(s') ds', \\ \mathbb{P}(\tilde{s}'|s, a; \beta) &= \tilde{\mathbb{P}}(\tilde{s}'; \beta) \int_{\mathcal{S}} \mathbb{P}(s'|s, a) \mathbb{P}(\tilde{s}'|s'; \beta) ds' \\ &\propto \tilde{\mathbb{P}}(\tilde{s}'; \beta) \exp(\varphi_\theta(s, a)^\top \nu_\theta(\tilde{s}'; \beta)). \end{aligned} \quad (39)$$

where the perturbation kernel is $\mathbb{P}(\tilde{s}'|s'; \beta) = \mathcal{N}(\sqrt{1-\beta}s', \beta I)$. Similar to the score matching case in section 4.3, the φ_θ is shared across different noise levels. As illustrated in Figure 2, when $\beta \rightarrow 0$, the perturbed distribution falls back to the original distributions; while for larger β , both the positive and negative distributions become smoother and increasingly overlap. This creates a more challenging classification task at higher noise levels, which acts as a powerful regularizer for the contrastive learning process. The final optimization objective, which we term *ranking-based perturbed NCE (RP-NCE)*, is an average of the NCE losses across all noise levels:

$$\ell_{\text{RP-NCE}}(\theta) = \frac{1}{MN} \sum_{m=1}^M \sum_{n=1}^N \log \frac{\exp(\varphi_\theta(s_n, a_n)^\top \nu_\theta(\tilde{s}'_{n,0}; \beta_m))}{\sum_{k=1}^K \exp(\varphi_\theta(s_n, a_n)^\top \nu_\theta(\tilde{s}'_{n,k}; \beta_m))}, \quad (40)$$

where $\tilde{s}'_{n,0}$ and $\tilde{s}'_{n,k}$ are sampled by perturbing the positive sample $s'_{n,0}$ and negative samples $s'_{n,k}$ with the Gaussian distribution $\mathbb{P}(\cdot|s'; \beta_k)$, respectively.

Algorithm 1 Online Reinforcement Learning with Spectral Representations

Initialize: replay buffer $\mathcal{D} = \emptyset$, policy π_ψ , representation networks φ_θ and ν_θ , reward network r_{θ, ξ_r} , and Q -value functions Q_{θ, ξ_1} and Q_{θ, ξ_2} according to the linear formulation (44), latent variable formulation (45) or energy-based formulation (46).

```

1: for  $t = 1, 2, \dots, T_{\text{total\_steps}}$  do
2:    $a_t \sim \pi(\cdot | s_t)$ 
3:    $r_t = r(s_t, a_t), s'_t \sim \mathbb{P}(\cdot | s_t, a_t)$ 
4:   (Optional) Compute bonus  $b(s_t, a_t)$ 
5:    $\mathcal{D} \leftarrow \mathcal{D} \cup \{(s_t, a_t, r_t, s'_t)\}$ 
6:   Update  $\varphi_\theta$ ,  $\nu_\theta$ , and  $r_{\theta, \xi_r}$  with spectral contrastive loss (27), variational learning (32), score matching (36), noise contrastive estimation (40) or its linear form (42), combined with the reward prediction loss (47)
7:   Update the value networks  $Q_{\theta, \xi_1}$  and  $Q_{\theta, \xi_2}$  with (48)
8:   Update the policy  $\pi_\psi$  with (49)
9: end for
Return  $\pi_\psi$ 

```

Remark (NCE for Linear Spectral Representations) CTRL [Zhang et al., 2022] leverages the NCE framework to derive linear spectral representations. It formulates the target density as:

$$\begin{aligned} \mathbb{P}(s' | s, a) &\propto \tilde{\mathbb{P}}(s') \varphi_\theta(s, a)^\top \nu_\theta(s, a) \\ \text{s.t. } \varphi_\theta(s, a)^\top \nu_\theta(s') &\geq 0, \quad \forall (s, a, s') \end{aligned} \tag{41}$$

The non-negativity constraint is necessary to ensure that $\mathbb{P}(s' | s, a)$ is a valid probability measure. The corresponding ranking-based perturbed NCE objective is:

$$\ell_{\text{RP-NCEL}}(\theta) = \frac{1}{MN} \sum_{m=1}^M \sum_{n=1}^N \log \frac{\varphi_\theta(s_n, a_n)^\top \nu_\theta(\tilde{s}'_{n,0}; \beta_m)}{\sum_{k=1}^K \varphi_\theta(s_n, a_n)^\top \nu_\theta(\tilde{s}'_{n,k}; \beta_m)}. \tag{42}$$

For spectral representations, CTRL uses $\phi_{\text{Linear}} \approx \varphi_{\theta^*}$. In practice, to enforce the non-negativity constraint in (41), we can activate the inner product in (42) with **SoftPlus**, a smoothed version of ReLU:

$$\text{SoftPlus}(x) = \log(1 + e^x). \tag{43}$$

Doing so will inevitably introduce non-linearity; however, we can encourage the model to operate in the linear regime of the **SoftPlus** function by adding a penalty term to push the inner product $\varphi_\theta(\cdot, \cdot)^\top \nu_\theta(\cdot)$ toward large positive values, such that $\text{SoftPlus}(x) \approx x$ and the linearity is preserved.

5 Reinforcement Learning with Spectral Representations

As established in Lemma 1, after we obtain the spectral representation, Q -value functions of any policy π can be expressed with one of the spectral representations: either ϕ_{Linear} , ϕ_{LV} , or ϕ_{EBM} . This connection inspires us to parameterize the Q functions on top of these representations, as we will detail below.

For the linear spectral representation where $\phi_{\text{Linear}} \approx \varphi_\theta$, Q functions can be parameterized as a linear function of the features with a weight vector $\xi \in \mathbb{R}^d$,

$$Q_{\theta, \xi}(s, a) = \varphi_\theta^\top \xi. \quad (44)$$

For the latent variable representation ϕ_{LV} , we can traverse the latent variables if \mathcal{Z} is discrete and finite or we can approximate Q -functions with Monte-Carlo estimations if \mathcal{Z} is continuous:

$$Q_{\theta, \xi}(s, a) = \langle \varphi_\theta(\cdot|s, a), \xi(\cdot) \rangle_{L_2} = \begin{cases} \sum_{i=1}^{|\mathcal{Z}|} \varphi_\theta(z_i|s, a) \xi(z_i) & \text{(discrete)} \\ \int_{\mathcal{Z}} \varphi_\theta(z|s, a) \xi(z) dz \approx \frac{1}{L} \sum_{l=1}^L \xi(z_l) & \text{(continuous)} \end{cases} \quad (45)$$

where $\xi : \mathcal{Z} \rightarrow \mathbb{R}$ is a function mapping the latent variable to a scalar value, typically parameterized by a neural network; $\{z_l\}_{l=1}^L$ are Monte-Carlo samples from $\varphi_\theta(\cdot|s, a)$.

For the energy-based representations ϕ_{EBM} , the parameterization is more complex due to its non-linear dependence on φ_θ , as defined in (22). This representation involves random Fourier features, $\zeta_N(\varphi(s, a))$, which we approximate using sinusoidal activations, i.e., a concatenation of $\sin(W_1^\top \varphi_\theta(s, a))$ and $\cos(W_1^\top \varphi_\theta(s, a))$. To account for the additional non-linearity from the term $\frac{1}{\langle \zeta_N(\varphi(s, a)), \mathbf{u} \rangle}$, we employ an additional network layer. This results in the following parameterization for the Q -function:

$$Q_{\theta, \xi} = \text{activ}(W_2 [\cos(W_1 \varphi_\theta(s, a)), \sin(W_1 \varphi_\theta(s, a))]^\top)^\top \eta, \quad (46)$$

where $\text{activ}(\cdot)$ is some nonlinear activation function and $\xi = (W_1, W_2, \eta)$ are learnable parameters optimized by the critic loss.

To also enforce the linear structure in the reward function (6), we parameterize a reward function r_{θ, ξ_r} using the same structure as Q -value functions, and include a reward prediction objective for the representation networks:

$$\ell_{\text{reward}}(\theta, \xi_r) = \mathbb{E}_{(s, a, s', r) \in \mathcal{D}} [(r_{\theta, \xi_r}(s, a) - r)^2]. \quad (47)$$

Following standard practice, we apply the *double Q-network trick* [Fujimoto et al., 2018] to stabilize learning and combat over-estimation bias. Specifically, we maintain two independent set of parameters ξ_1, ξ_2 and their exponential moving average (EMA) version $\bar{\theta}_1, \bar{\theta}_2$, and update the Q -value functions using the standard TD learning objective:

$$\ell_{\text{critic}}(\xi_1, \xi_2) = \mathbb{E}_{(s, a, r, s') \sim \mathcal{D}} \left[\sum_{i \in \{1, 2\}} \left(r + \gamma \mathbb{E}_{a' \sim \pi} \left[\min_{j \in \{1, 2\}} Q_{\theta, \xi_j}(s', a') \right] - Q_{\theta, \xi_i} \right)^2 \right]. \quad (48)$$

The policy is then updated by maximizing the expected Q -value:

$$\ell_{\text{policy}}(\pi) = \mathbb{E}_{s \sim \mathcal{D}, a \sim \pi(\cdot|s)} \left[\min_{i \in \{1, 2\}} Q_{\theta, \xi_i}(s, a) \right]. \quad (49)$$

Algorithm 1 presents the pseudo-code of online RL algorithms equipped with spectral representations, where the data collection, policy optimization, and representation learning are performed

simultaneously. Note that the training of critics and representation networks is decoupled, *i.e.*, the TD learning objective ℓ_{critic} is not used to train φ_θ and ν_θ . In fact, the framework of spectral representations can be readily integrated into a wide range of reinforcement learning algorithms, including those designed for offline scenarios and visual-input tasks. This showcases the wide applicability of spectral representations.

Theoretical Analysis

The optimistic exploration with spectral representation has been justified rigorously in [Ren et al., 2023a,b], which we briefly introduce here. We first make the following assumptions about the candidate class and normalization conditions, which are common among similar analysis.

Assumption 1 *Let $|\mathcal{P}| < \infty$ and $\phi \in \mathcal{P}, \mu \in \mathcal{P}$. For $\forall (s, a) \in \mathcal{S} \times \mathcal{A}$ and $\forall s' \in \mathcal{S}$, $\phi(s, a) \in \mathcal{H}_k$ and $\mu(s') \in \mathcal{H}_k$ for some RKHS \mathcal{H}_k with kernel k .*

Unlike the linear MDP case [Jin et al., 2020, Uehara et al., 2021], we consider representations in the RKHS \mathcal{H}_k , which includes all formulations in Section 3 and provides an abstraction. For example, the energy-based formulation can be recognized as specifying k as the Gaussian kernel (17), while the linear formulation can be recovered using a linear kernel.

Assumption 2 *(Normalizing Conditions) Let kernel k be defined on a compact metric space \mathcal{Z} with the Lebesgue measure μ if \mathcal{Z} is continuous, and $\int_{\mathcal{Z}} k(z, z) dz \leq 1$. For $\forall (\phi, \mu) \in \mathcal{P}$, $\|\phi(s, a)\|_{\mathcal{H}_k} \leq 1$. Besides, $\forall g : \mathcal{S} \rightarrow \mathbb{R}$ such that $\|g\|_\infty \leq 1$, we have $\|\int_{\mathcal{S}} \mu(s') g(s') ds'\| \leq C$.*

Assumption 3 *(Eigenvalue Decay Conditions) For the reproducing kernel, we assume μ_i , the i -th eigenvalue of the operator $T_k : L_2(\mu) \rightarrow L_2(\mu)$, $T_k f = \int_{\mathcal{Z}} f(z') k(z, z') d\mu(z')$, satisfies one of the following conditions:*

- β -finite spectrum: $\mu_i = 0$ for $\forall i > \beta$ where β is a positive integer;
- β -polynomial decay: $\mu_i \leq C_0 i^{-\beta}$, where C_0 is an absolute constant and $\beta \geq 1$;
- β -exponential decay: $\mu_i \leq C_1 \exp(-C_2 i^\beta)$, where C_1, C_2 are absolute constants and $\beta > 0$.

Most common kernels satisfy the above decay conditions. For example, the linear and polynomial kernels satisfy the β -finite spectrum condition, while the Gaussian kernel satisfies β -exponential decay. Finally, we present the sample complexity bound for online reinforcement learning.

Theorem 3 *(PAC Guarantee for Online Reinforcement Learning) Assume the reproducing kernel k satisfies the eigenvalue decay conditions in Assumption 3. With a proper choice of exploration bonus function $\hat{b}_n(s, a)$, the optimistic version of our algorithm 2 can yield an ϵ -optimal policy with probability at least $1 - \delta$ after interacting with the environment for $N = \text{poly}(C, |\mathcal{A}|, (1 - \gamma)^{-1}, \epsilon, \log(|\mathcal{P}|/\delta))$ episodes.*

This theorem and its proof largely follow Theorem 4 in Ren et al. [2023a], except that the bonus functions \hat{b}_n are defined with the RKHS inner product $\langle \cdot, \cdot \rangle_{\mathcal{H}_k}$, rather than $\langle \cdot, \cdot \rangle_{L_2(\mu)}$. We refer interested readers to Appendix E of Ren et al. [2023a] for a detailed proof.

6 Spectral Representations in Partially Observable MDPs

In this section, we demonstrate that the framework of spectral representations can be seamlessly extended to partially observable MDPs (POMDPs), leading to the first practical algorithm that can provably solve a subclass of POMDPs. Following [Efroni et al. \[2022\]](#), a POMDP is defined by the tuple $\langle \mathcal{S}, \mathcal{A}, \mathcal{O}, \mathbb{P}, \mathbb{O}, r, \gamma, d_0 \rangle$, where \mathcal{S} , \mathcal{A} , and \mathcal{O} are the state, action, and observation spaces, $r : \mathcal{O} \times \mathcal{A} \rightarrow \mathbb{R}$ is the reward function, $\mathbb{P} : \mathcal{S} \times \mathcal{A} \rightarrow \Delta(\mathcal{S})$ is the transition probability over the latent states, and $\mathbb{O} : \mathcal{S} \rightarrow \Delta(\mathcal{O})$ is the emission probability that governs the observation an agent will receive given the system state.

By introducing the belief function $b(\cdot) : (\mathcal{O} \times \mathcal{A})^t \times \mathcal{O} \rightarrow \Delta(\mathcal{S})$ that maps the observation and action history to a distribution over the system states, POMDPs can be converted into equivalent belief state MDPs $\mathcal{M}_b = \langle \mathcal{B}, \mathcal{A}, \mathbb{P}_b, r_b, \gamma, d_{b,0} \rangle$. Here, $\mathcal{B} \subseteq \Delta(\mathcal{S})$ is the space of beliefs, $d_{b,0}(\cdot) = \int \int d_0(s_0) \mathbb{O}(o_0|s_0) b(\cdot|o_0) ds_0 do_0$, and

$$\begin{aligned} \mathbb{P}_b(b_{t+1}|b_t, a_t) = \\ \int \int \int \mathbf{1}_{b_{t+1}=b(o_{1:t+1}, a_t)} \mathbb{O}(o_{t+1}|s_{t+1}) \mathbb{P}(s_{t+1}|s_t, a_t) b_t(s_t|o_{1:t}, a_{t-1}) ds_t ds_{t+1} do_{t+1}. \end{aligned} \quad (50)$$

The value functions, $V^\pi(b_t)$ and $Q^\pi(b_t, a_t)$, can then be defined over these belief states. However, the belief state MDPs equivalence does not induce a practical algorithm, since the belief states are not directly observed and are dependent on the entire history. Consequently, to reduce the statistical complexity of learning, we consider a special class of POMDPs with the following structure.

Definition 4 (*L*-decodability [[Efroni et al., 2022](#)]) Define

$$\begin{aligned} x_t \in \mathcal{X} := (\mathcal{O} \times \mathcal{A})^{L-1} \times \mathcal{O}, \\ x_t = (o_{t-L+1}, a_{t-L+1}, \dots, o_t), \end{aligned} \quad (51)$$

a POMDP is *L*-decodable if there exists a decoder $p : \mathcal{X} \rightarrow \Delta(\mathcal{S})$ such that $p(x_t) = s_t$.

Intuitively, *L*-decodability implies that the *L*-step history window serves as a sufficient statistic for the state s_t . We note that the *L*-decodability is a plausible assumption that commonly holds in practical decision-making scenarios. For example, in visual RL, although a single frame may be insufficient to capture the full system state (e.g., velocity of the robot), stacking consecutive frames effectively compensates for this partial observability and has become the de facto practice in modern visual RL algorithms [[Mnih et al., 2013](#), [Yarats et al., 2021a](#)].

Most importantly, the *L*-decodability assumption eliminates the dependence on earlier trajectory history in transition probabilities, allowing us to define value functions directly over this windowed history, $Q^\pi(x_t, a_t)$, which satisfy the *L*-step Bellman equation:

$$Q^\pi(x_t, a_t) = \mathbb{E}_{x_{t+1:t+L} \sim \mathbb{P}^\pi(\cdot|x_t, a_t)} \left[\sum_{i=0}^{L-1} \gamma^i r_{t+i} + \gamma^L V^\pi(x_{t+L}) \right], \quad (52)$$

where $V^\pi(x_{t+L})$ is independent of (x_t, a_t) thanks to the *L*-decodability property. To further eliminate the dependence on x_t in $x_{t+1:t+L-1}$, we employ the *moment matching policy* [[Efroni et al., 2022](#)] $\tilde{\pi}$, which conditions solely on (x_t, a_t) but generates the same *L*-step observation distribution as π (proof provided in [Zhang et al.](#), Appendix C). In this way, if we consider the spectral

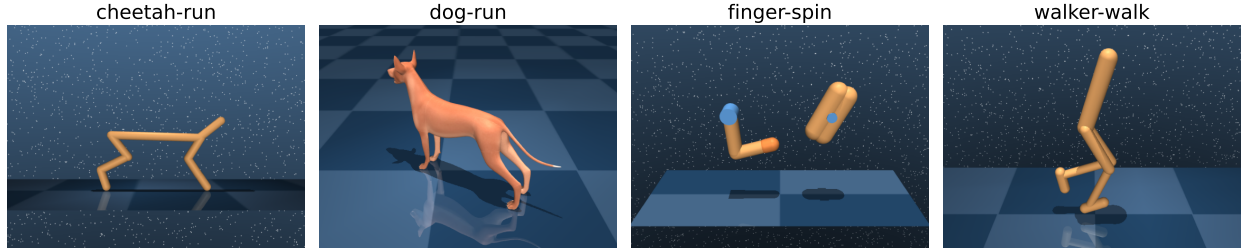


Figure 3: Visual illustrations of four representative tasks from the DMControl Benchmark.

decomposition of the L -step transition and reward:

$$\begin{aligned} \mathbb{P}_L^\pi(x_{t+L}|x_t, a_t) &= \langle \phi(x_t, a_t), \boldsymbol{\mu}^{\tilde{\pi}}(x_{t+L}) \rangle_{\mathcal{H}}, \\ r_L^\pi(x_t, a_t) &= \sum_{i=0}^{L-1} \gamma^i r_{t+i} = \langle \phi(x_t, a_t), \boldsymbol{\theta}_r^{\tilde{\pi}} \rangle_{\mathcal{H}}, \end{aligned} \quad (53)$$

then it follows that $Q^\pi(x_t, a_t) = \langle \phi(x_t, a_t), \boldsymbol{\theta}_r^{\tilde{\pi}} + \gamma^L \boldsymbol{\mu}^{\tilde{\pi}}(x_{t+L}) \rangle$, making $\phi(x_t, a_t)$ the spectral representation that can sufficiently express the Q -value function. Consequently, all three formulations in Section 3.2 and the representation learning methods in Section 4 extend naturally to such L -step transition and rewards. For example, noise contrastive estimation now parameterizes the representation networks $\phi(o_{t-L+1:t}, a_t)$ and $\boldsymbol{\nu}(o_{t+1:t+L})$ using L consecutive frames as input and for contrastive learning. For prediction-based approaches such as variational learning, since predicting all L frames may be computationally expensive, we can also work with predicting every single frame as an approximation. Finally, the RL algorithmic implementations and theoretical characterizations in Section 5 also carry over to this setting, yielding a family of practical and theoretically grounded algorithms for solving POMDPs.

7 Empirical Evaluations

In this section, we evaluate the effectiveness of spectral representation-based RL algorithms using the widely recognized DeepMind Control (DMControl) Suite [Tassa et al., 2018]. Our experiments are designed to answer two primary questions: 1) whether learning spectral representations improves policy optimization, and 2) how different formulations and learning methods for these representations compare against each other and state-of-the-art baselines. To fulfill this, we conduct our evaluation on over 20 distinct tasks from the suite, encompassing both low-dimensional proprioceptive states and high-dimensional visual inputs. Rendered illustrations of these tasks are shown in Figure 3.

We implement and compare the following representative instantiations of the spectral representation framework:

1. **Speder** [Ren et al., 2023b], which employs a linear formulation and learns representations ϕ_{Linear} via spectral contrastive learning (27);
2. **LV-Rep** [Ren et al., 2023a], which trains a latent variable spectral representation ϕ_{LV} through variational learning (32);

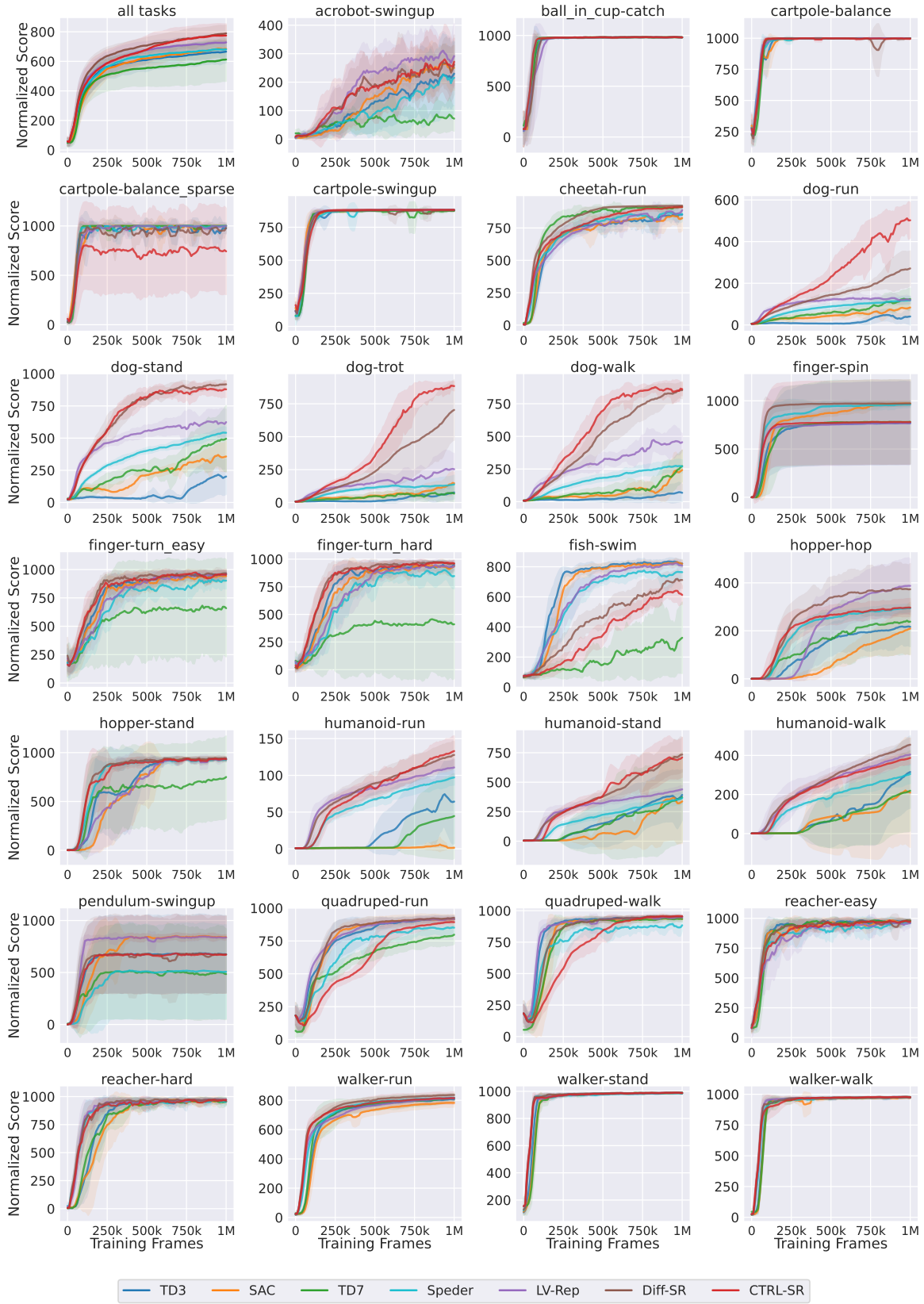


Figure 4: Curves of average episode return on DMControl Suite with proprioceptive inputs, with the first plot depicting the averaged performance across all 27 tasks. All curves are smoothed with a window of 5 for clearer presentation.

3. **Diff-SR** [Shribak et al., 2024], which utilizes an energy-based formulation ϕ_{EBM} optimized with score matching (36);
4. **CTRL-SR**, which improves **CTRL** [Zhang et al., 2022] by using ranking-based perturbed NCE (40) as its representation learning objectives. Note that it also employs the energy-based representations ϕ_{EBM} instead of the ϕ_{Linear} in **CTRL**.

To ensure a fair and controlled comparison, each method is built upon a fine-tuned implementation of the popular TD3 algorithm. We hold all hyperparameters constant across the tasks for each method. This setup isolates the impact of representation learning from that coming from hyperparameter tuning efforts. A detailed description of the hyperparameters and experimental setup is provided in the subsequent sections as well as in Appendix B.

7.1 Results with Proprioceptive Observations

Proprioceptive observations refer to the sensory information that an agent receives about its own internal state, such as the body’s position, orientation, and velocity. In DMControl, proprioceptive observations offer a comparatively compact description of the system state, with a dimensionality that scales according to the robot’s morphological complexity. For example, the simple **pendulum-*** task uses a 3-dimensional observation space, comprising the Cartesian coordinates of the pendulum tip and its angular velocity. In contrast, **dog-*** tasks use a 223-dimensional observation space to encode the complete state of its torso and joints. Collectively, these tasks form a comprehensive evaluation with a wide spectrum of dynamics complexities, allowing for a thorough evaluation of an algorithm’s ability to scale to high-dimensional control problems.

For our baselines, we select two model-free algorithms, TD3 [Fujimoto et al., 2018] and SAC [Haarnoja et al., 2018]. We also include TD7 [Fujimoto et al., 2023], a recent TD3 variant that incorporates representation learning, to provide a strong comparison. A consistent training and evaluation protocol is applied to all algorithms and tasks. Each agent interacts with the environment for 1 million frames, with each action being repeated for two consecutive frames (*i.e.*, an action repeat of two frames). The agent’s policy is updated every two frames, which amounts to 500,000 gradient steps in total. Performance is evaluated every 10,000 frames by averaging the returns over 10 episodes. To ensure statistical reliability, we report the mean and standard deviation of these evaluation scores across 5 independent runs, each initialized with a different random seed.

Figure 4 displays the curves of returns with respect to the environment timesteps, with the first plot providing an aggregated performance summary across all 27 tasks. Although purely model-free algorithms like TD3 and SAC can readily solve most tasks, they struggle to scale to environments with high-dimensional tasks. Notably, on complex tasks such as **dog-trot** and **humanoid-stand**, they fail to achieve meaningful performances. This outcome highlights a key limitation of model-free RL: its difficulty in leveraging the structural information embedded within the data and in developing temporal abstractions when relying solely on reward signals.

Representation-based methods, with the exception of TD7, consistently outperform their model-free counterpart, TD3. These improvements are particularly pronounced on the more complex **dog-*** tasks and **humanoid-*** tasks, where algorithms using spectral representations achieve significant gains. Among the spectral representation algorithms, a clear performance hierarchy emerged. **Speder** generally performed the poorest, followed by **LV-Rep**, with the two energy-based methods, **Diff-SR** and **CTRL-SR**, achieving the best results. This is likely due to the inherent limitation of linear spectral representations, as finite-dimensional representations may cause information loss

when representing both the dynamics and the value functions. For the latent variable version, although this method is more flexible by using infinite-dimensional representations, the Monte-Carlo approximation used to represent the Q -value functions can, however, introduce high variance into training. Finally, the energy-based approach is the most flexible one, since 1) the representations are implicitly infinite-dimensional due to the Gaussian kernel transformation, and 2) it introduces additional learning parameters that are trained by the critic loss, allowing it to offer the best performance among all the methods evaluated.

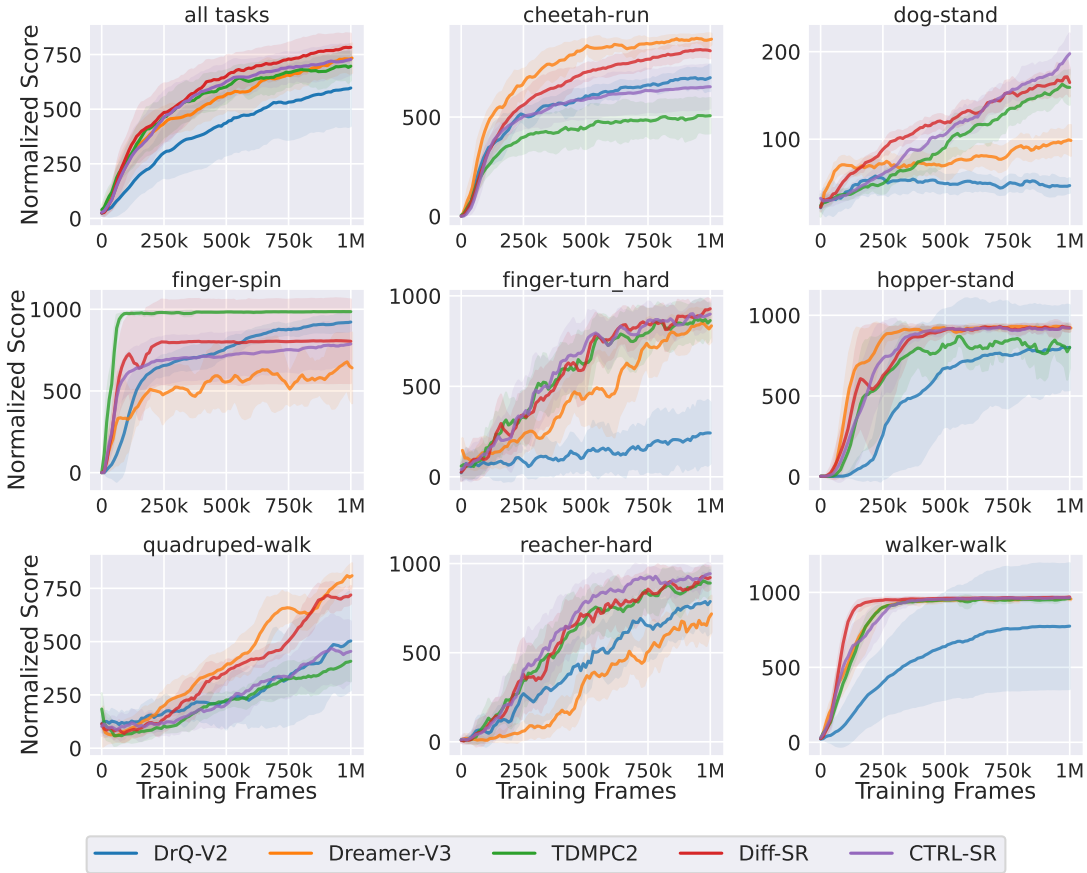


Figure 5: Curves of average episode return on DMControl Suite with visual inputs, with the first plot depicting the averaged performance across all 8 tasks. All curves are smoothed with a window of 5 for clearer presentation.

7.2 Results with Visual Observations

To further demonstrate the benefits of spectral representations, we evaluate our methods on a subset of 8 tasks from the DMControl Suite with visual observations. At each timestep, the agent receives a rendered 84×84 third-person view of its current state instead of receiving the ground-truth proprioceptive state. To compensate for the partial observability inherent in single frames, we follow the standard practice of stacking 3 consecutive frames to form the agent’s observation. The combination of high-dimensional visual data and complex dynamics provides a rigorous benchmark

for assessing the capabilities of each algorithm. Besides, the action repeat is kept as 2 frames for all algorithms, and the evaluation protocol is the same as that in Section 7.1.

For the baseline algorithms, we include: 1) DrQ-V2 [Yarats et al., 2021a], a competitive model-free visual RL algorithm which employs data augmentation to enhance the visual encoders; 2) TDMPC2 [Hansen et al., 2023], a model-based algorithm that performs model predictive control during sampling; and 3) Dreamer-V3 [Hafner et al., 2023], the state-of-the-art model-based algorithm that employs an RSSM structured model for agent training.

We implemented the best-performing methods, namely **Diff-SR** and **CTRL-SR**, for this setting. To handle the visual input, we adopt a convolutional visual encoder to extract a lower-dimensional latent vector from the stacked frames, and the representation networks treat the extracted latent vectors as states. For **CTRL-SR**, the visual encoder is jointly optimized along with the representation networks, while for **Diff-SR**, we found that joint optimization may lead to representation collapse, a similar phenomenon that is also observed by other representation learning methods [Grill et al., 2020, Bardes et al., 2021]. Thus, we decided to train the visual encoder using a variance-regularized reconstruction objective. More details about the implementation can be found in Appendix B.

The learning curves are presented in Figure 5, with the first plot presenting an aggregated result across 8 tasks. As a baseline, DrQ-V2, which relies solely on visual data augmentation to regularize the visual encoder, consistently underperforms compared to dynamics-informed methods. In contrast, spectral representation-based methods, despite also being model-free, achieve performance comparable to that of leading model-based algorithms. Notably, they even outperform these approaches on challenging tasks such as **dog-stand**. Furthermore, Figure 6 compares the training time required by each algorithm. Despite utilizing larger network architectures, both **Diff-SR** and **CTRL-SR** require significantly less training time than model-based competitors, since the representation-based method avoids the costly model-based planning procedure. Collectively, these observations validate that spectral representations provide a powerful and efficient foundation for policy optimization.

7.3 Ablation Study and Analysis

Representation Dimension. Despite sharing the linear structure, different formulations in Section 3 demonstrate different scaling behaviors. As shown in figure 7, we compare **Speder** and **CTRL-SR** as representatives for the linear and energy-based formulation, respectively. While both methods improve with a higher representation dimension d , the energy-based formulation achieves better final performance under the same capacity and continues to scale up as the dimension increases. We hypothesize this is because energy-based models implicitly learn an infinite-dimensional feature map. While this map is ultimately truncated to a finite dimension using Random Fourier Features, the fact that these frequencies are selected by the critic function better facilitates the

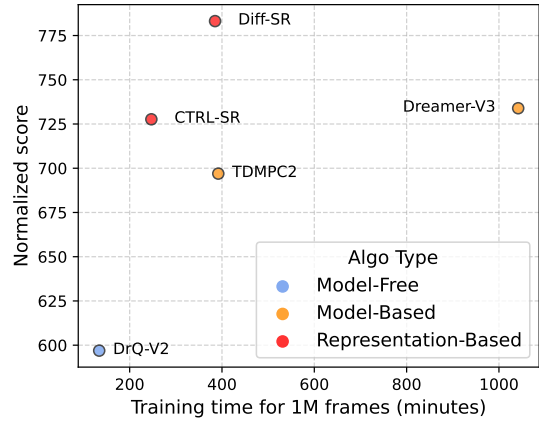


Figure 6: Runtime comparison on tasks with visual observations.

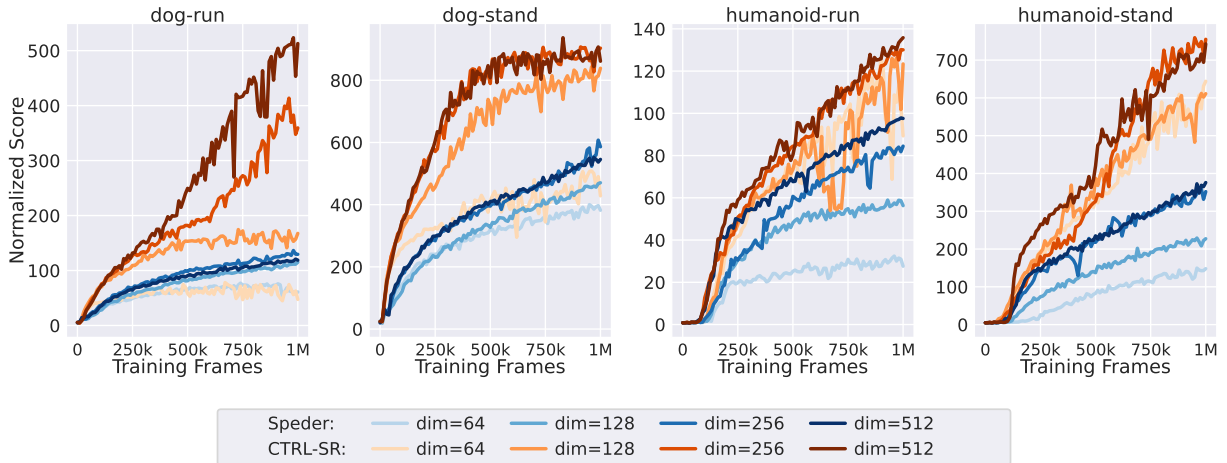


Figure 7: Performance of **Speder** and **CTRL-SR** with different representation dimensions.

downstream policy optimization.

Noise Perturbation. Both **Diff-SR** and **CTRL-SR** utilize noise perturbation to improve representation learning, albeit for different reasons. **Diff-SR** trains its network to denoise state transitions, whereas **CTRL-SR** uses noise to prevent representation collapse due to an overly simple contrastive task. In Figure 8, we investigate how performance changes with varying noise levels. We observe that, generally, there is no significant performance variation across different noise magnitudes. However, for **CTRL-SR**, performance degrades drastically in the complete absence of noise. This result showcases the efficacy of the noise perturbation technique, particularly for stabilizing the contrastive learning process.

Coupled Training with Critic Objectives. In our proposed algorithm 1, the representation network is trained exclusively using representation learning objectives (line 6). Our theory suggests that representations derived from the transition operator decomposition are sufficient for expressing the Q -value function, thereby eliminating the need to use critic objectives to further tune the network. However, since we are working with finite-dimensional approximations of the spectral representations, it is likely that useful dimensions for representing Q -value functions are truncated. Therefore, we also evaluate a variant that couples the critic and representation learning objectives. This approach can be viewed as using the representation objective as a regularization term, while the critic objective is used to train both the representation network and the Q -value function. As observed in Figure 9, the variants that combine both objectives demonstrate uniform improvement across all evaluated tasks.

8 Related Work

8.1 Reinforcement Learning with Representation Learning

Given the advancements in self-supervised learning (SSL) and the inherent challenges of reinforcement learning (RL) in high-dimensional spaces, there is growing interest in leveraging representa-

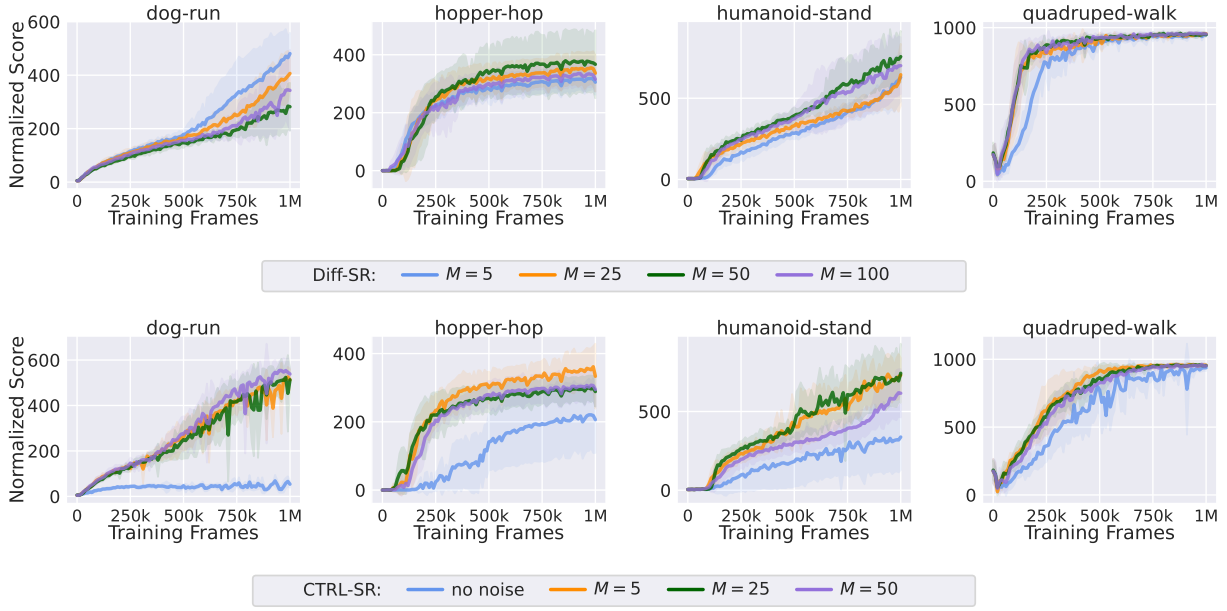


Figure 8: Performance of Diff-SR and CTRL-SR with different number of noises.

tion learning to improve RL efficiency. A straightforward application of this approach has been in visual RL, where agents perceive the environment through camera images that often contain redundant information. Many established visual representation techniques, including data augmentation [Yarats et al., 2021b,a], observation reconstruction [Yarats et al., 2021c], and contrastive representation learning [Laskin et al., 2020], can be readily integrated to derive compact features for the learning.

In parallel to visual representation learning, a long-standing topic in RL is learning *temporal* representations that encode system behavior and facilitate long-term planning. Among them, successor features [Dayan, 1993, Kulkarni et al., 2016, Barreto et al., 2017] and forward-backward representations [Touati and Ollivier, 2021] learn to summarize the long-term consequences of actions and can potentially adapt to different reward functions by applying the learned representations. Methods based on bisimulation metrics [Ferns et al., 2004, Gelada et al., 2019, Castro, 2020, Liao et al., 2023] quantify the behavioral similarity between states and learn representations that group equivalent states together. Inspired by model-based approaches, a large body of work [Munk et al., 2016, Lee et al., 2020, Guo et al., 2020, Schwarzer et al., 2020, McInroe et al., 2021, Yu et al., 2022, Tang et al., 2023, Kim et al., 2025, Fujimoto et al., 2023, 2025, Assran et al., 2025] learns representations by predicting future system states, either directly from observations or in a latent space. The spectral representation framework [Ren et al., 2022, 2023a, Zhang et al., 2022, Ren et al., 2023b, Shribak et al., 2024] addressed in this paper is closely related to these methods, especially Fujimoto et al. [2025], which learn a linear, self-predictive latent representation of states and actions and build the Q-value function upon them. To see this connection, the second term of the spectral contrastive loss in (27) is equivalent to predicting the representation of the next state under deterministic MDPs and certain normalization conditions on the representations. The variational learning objective in (32) can also be cast as a non-linear extension of the latent representation prediction problem. Finally, the contrastive learning objective used by CTRL-SR has

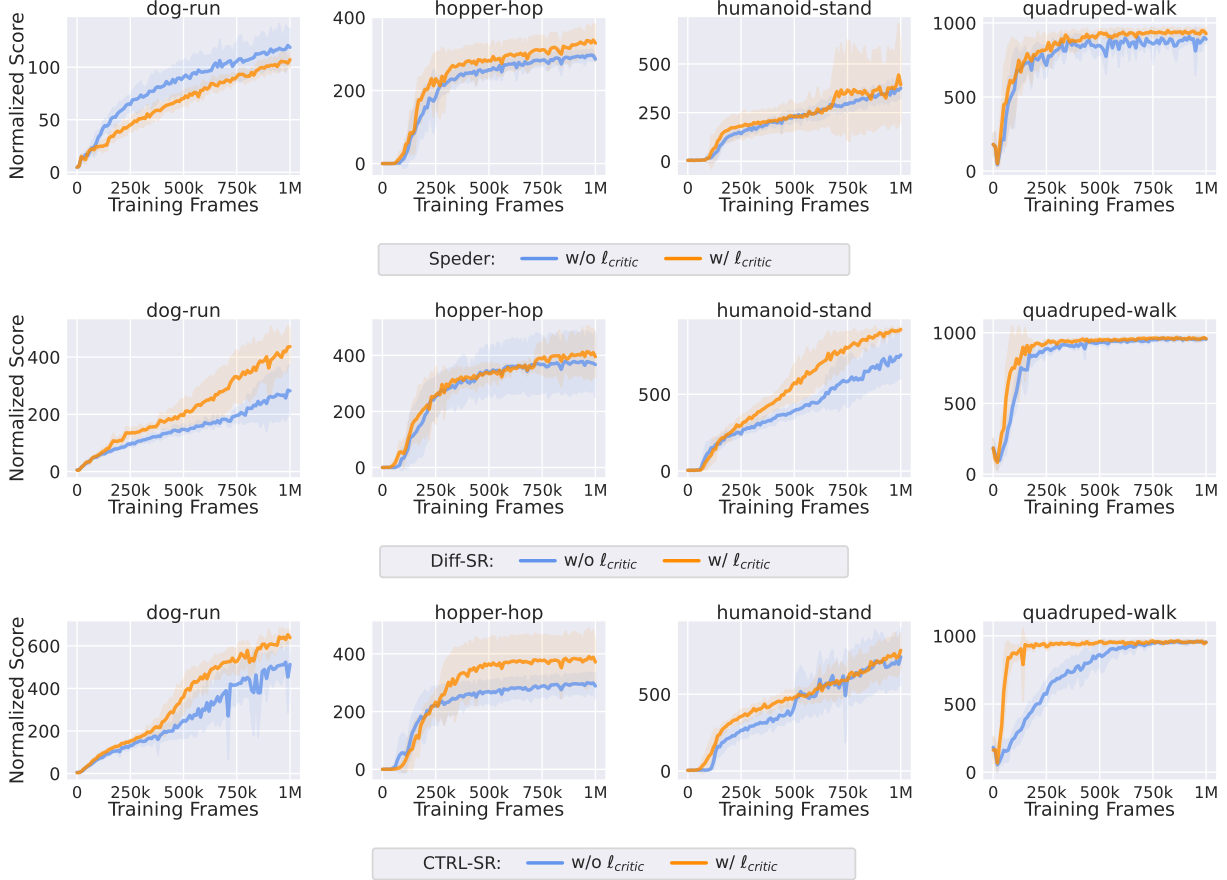


Figure 9: Performance of Speder, Diff-SR, and CTRL-SR with or without using ℓ_{critic} for representation learning.

also been employed to extract temporal abstractions of the system by distinguishing ground-truth state transitions from faked ones [Oord et al., 2018, Anand et al., 2019, Stooke et al., 2021, Zheng et al., 2023].

While the learning objectives share many similarities, spectral representations go beyond merely capturing the predictive structure. By exploiting the spectrum structure of the dynamics, spectral representations are distinguished from these alternatives by their unique connection to the Q -value functions, which we have demonstrated in Theorem 3 is crucial for exploration design and efficient learning.

8.2 Model-Based Reinforcement Learning

Model-based reinforcement learning (RL) learns a model of the environment dynamics from observed state transitions and rewards, and then leverages it to facilitate policy optimization [Luo et al., 2024]. One predominant approach treats the approximated model as a surrogate of the true environment, allowing the agent to generate synthetic trajectories through fictitious interaction [Chua et al., 2018, Luo et al., 2018, Janner et al., 2019, Yu et al., 2020]. In essence, these

synthetic trajectories augment the real-world experience by illustrating counterfactuals, depicting what might have happened if different actions were taken, thereby reducing the demand for trial-and-error in the real world. In terms of modeling, various generative models or architectures have been explored, spanning from Gaussian processes [Kamthe and Deisenroth, 2018], neural network parameterized deterministic or stochastic models [Chua et al., 2018, Luo et al., 2018, Hansen et al., 2022, 2023, Zhou et al.], recurrent state space models (RSSMs) [Hafner et al., 2019b,a, 2020, 2023], transformers [Chen et al., 2022a, Micheli et al., 2022], energy-based models [Chen et al., 2024], and diffusion models [Ding et al., 2024, Alonso et al., 2024]. Beyond the intricate design of the model architecture, the planning process itself also warrants careful design to mitigate the risk of generating unrealistic trajectories. This is because errors in state prediction can accumulate with long planning horizons, a phenomenon known as the *compounding error*. To manage this error, common strategies include branch rollout [Janner et al., 2019], early truncation [Kidambi et al., 2020], or reward penalty [Yu et al., 2020, Sun et al., 2023]. In contrast, our proposed methods adopt a similar way to extract dynamics-informed representations from experiences but completely obviate the need for planning, thereby achieving greater computational efficiency.

Apart from learning the dynamics model with task-specific interaction data, there has been a notable trend in adapting foundation models for dynamics prediction. This approach, first proposed as *world models* [Ha and Schmidhuber, 2018], has been revitalized due to the advances in generative models. V-JEPA 2-AC [Assran et al., 2025] and DINO-world [Baldassarre et al., 2025] adopt similar approaches, by first pre-training visual encoders on large-scale video or image datasets, and subsequently post-training a predictive model with action-annotated datasets for control and planning. To even eliminate the need for such action-annotated datasets, Genie [Bruce et al., 2024] infers latent actions from unlabelled videos and learns a world model modulated by such latent actions jointly. While substantial progress has been made on the visual pre-training, the dynamics modeling component remains comparatively underexplored. Spectral representations help fill this gap by offering a principled and diverse control-oriented perspective that can be paired with existing high-quality visual representations.

9 Closing Remarks

In this survey, we systematically review the advances in spectral representations for efficient reinforcement learning. We elucidate the core design choices in this framework, namely the specific formulation of the spectral representations and the choice of learning algorithm. Focusing on the online reinforcement learning setting, we implement representative methods and compare existing methods under a fair protocol. This provides a quantitative comparison of these algorithms both against one another and against standard baselines.

We believe our review and experiments reveal only a fraction of the potential held by spectral representations. Beyond online reinforcement learning, spectral representations provide a natural way to leverage offline [Levine et al., 2020] or passive [Ghosh et al., 2023] interaction data, facilitating sample-efficient online adaptation. Unlike skill-based pre-training that often requires intricate algorithm design and is heavily dependent on the behavior policy, pre-training spectral representations only requires access to transition data, thus possessing superior transferability and generalization [Ren et al., 2023b, Wang et al., 2025]. Furthermore, spectral representations can be readily extended to various RL scenarios, such as off-policy evaluation [Hu et al., 2024], multi-agent RL [Ren et al., 2024], and goal-conditional RL [Eysenbach et al., 2022], by identifying the spectral

structure within the system dynamics and connecting them to the components in RL pipeline.

Outside the scope of reinforcement learning, spectral representation also casts a novel perspective on modular designs of modern generative models like large language models (LLMs) and diffusion models. As these models are also pre-trained on large-scale, unlabeled datasets, they also yield instrumental representations for downstream tasks like fine-tuning or post-training. We hope this survey can inspire further exploration of this perspective and foster the design of more efficient and robust algorithms.

Acknowledgements

This paper is supported by NSF AI institute: 2112085, NSF ECCS-2401390, NSF ECCS-2401391, ONR N000142512173, and NSF IIS2403240.

References

Alekh Agarwal, Sham Kakade, Akshay Krishnamurthy, and Wen Sun. Flambe: Structural complexity and representation learning of low rank mdps. *Advances in Neural Information Processing Systems (NeurIPS)*, 33:20095–20107, 2020.

Shipra Agrawal and Randy Jia. Optimistic posterior sampling for reinforcement learning: worst-case regret bounds. *Advances in Neural Information Processing Systems (NeurIPS)*, 30, 2017.

Eloi Alonso, Adam Jolley, Vincent Micheli, Anssi Kanervisto, Amos J Storkey, Tim Pearce, and François Fleuret. Diffusion for world modeling: Visual details matter in atari. *Advances in Neural Information Processing Systems (NeurIPS)*, 37:58757–58791, 2024.

Ankesh Anand, Evan Racah, Sherjil Ozair, Yoshua Bengio, Marc-Alexandre Côté, and R Devon Hjelm. Unsupervised state representation learning in atari. *Advances in Neural Information Processing Systems (NeurIPS)*, 32, 2019.

Mido Assran, Adrien Bardes, David Fan, Quentin Garrido, Russell Howes, Matthew Muckley, Ammar Rizvi, Claire Roberts, Koustuv Sinha, Artem Zhulus, et al. V-jepa 2: Self-supervised video models enable understanding, prediction and planning. *arXiv preprint arXiv:2506.09985*, 2025.

Peter Auer, Thomas Jaksch, and Ronald Ortner. Near-optimal regret bounds for reinforcement learning. *Advances in Neural Information Processing Systems (NeurIPS)*, 21, 2008.

Mohammad Gheshlaghi Azar, Ian Osband, and Rémi Munos. Minimax regret bounds for reinforcement learning. In *International Conference on Machine Learning (ICML)*, pages 263–272. PMLR, 2017.

Federico Baldassarre, Marc Szafraniec, Basile Terver, Vasil Khalidov, Francisco Massa, Yann LeCun, Patrick Labatut, Maximilian Seitzer, and Piotr Bojanowski. Back to the features: Dino as a foundation for video world models. *arXiv preprint arXiv:2507.19468*, 2025.

Adrien Bardes, Jean Ponce, and Yann LeCun. Vicreg: Variance-invariance-covariance regularization for self-supervised learning. *arXiv preprint arXiv:2105.04906*, 2021.

André Barreto, Will Dabney, Rémi Munos, Jonathan J Hunt, Tom Schaul, Hado P van Hasselt, and David Silver. Successor features for transfer in reinforcement learning. *Advances in Neural Information Processing Systems (NeurIPS)*, 30, 2017.

Christopher Berner, Greg Brockman, Brooke Chan, Vicki Cheung, Przemysław Debiak, Christy Dennison, David Farhi, Quirin Fischer, Shariq Hashme, Chris Hesse, et al. Dota 2 with large scale deep reinforcement learning. *arXiv preprint arXiv:1912.06680*, 2019.

Jake Bruce, Michael D Dennis, Ashley Edwards, Jack Parker-Holder, Yuge Shi, Edward Hughes, Matthew Lai, Aditi Mavalankar, Richie Steigerwald, Chris Apps, et al. Genie: Generative interactive environments. In *International Conference on Machine Learning (ICML)*, 2024.

Pablo Samuel Castro. Scalable methods for computing state similarity in deterministic markov decision processes. In *Proceedings of the AAAI Conference on Artificial Intelligence (AAAI)*, volume 34, pages 10069–10076, 2020.

Chang Chen, Yi-Fu Wu, Jaesik Yoon, and Sungjin Ahn. Transdreamer: Reinforcement learning with transformer world models. *arXiv preprint arXiv:2202.09481*, 2022a.

Changyou Chen, Jianyi Zhang, Yi Xu, Liqun Chen, Jiali Duan, Yiran Chen, Son Tran, Belinda Zeng, and Trishul Chilimbi. Why do we need large batchsizes in contrastive learning? a gradient-bias perspective. *Advances in Neural Information Processing Systems (NeurIPS)*, 35:33860–33875, 2022b.

Ruifeng Chen, Chengxing Jia, Zefang Huang, Tian-Shuo Liu, Xu-Hui Liu, and Yang Yu. Offline transition modeling via contrastive energy learning. In *International Conference on Machine Learning (ICML)*, 2024.

Kurtland Chua, Roberto Calandra, Rowan McAllister, and Sergey Levine. Deep reinforcement learning in a handful of trials using probabilistic dynamics models. *Advances in Neural Information Processing Systems (NeurIPS)*, 31, 2018.

Bo Dai, Albert Shaw, Lihong Li, Lin Xiao, Niao He, Zhen Liu, Jianshu Chen, and Le Song. Sbeed: Convergent reinforcement learning with nonlinear function approximation. In *International conference on machine learning*, pages 1125–1134. PMLR, 2018.

Christoph Dann and Emma Brunskill. Sample complexity of episodic fixed-horizon reinforcement learning. *Advances in Neural Information Processing Systems (NeurIPS)*, 28, 2015.

Peter Dayan. Improving generalization for temporal difference learning: The successor representation. *Neural computation*, 5(4):613–624, 1993.

Jonas Degrave, Federico Felici, Jonas Buchli, Michael Neunert, Brendan Tracey, Francesco Carpanese, Timo Ewalds, Roland Hafner, Abbas Abdolmaleki, Diego de Las Casas, et al. Magnetic control of tokamak plasmas through deep reinforcement learning. *Nature*, 602(7897):414–419, 2022.

Marc Deisenroth and Carl E Rasmussen. Pilco: A model-based and data-efficient approach to policy search. In *International Conference on machine learning (ICML)*, pages 465–472, 2011.

Zihan Ding, Amy Zhang, Yuandong Tian, and Qinqing Zheng. Diffusion world model: Future modeling beyond step-by-step rollout for offline reinforcement learning. *arXiv preprint arXiv:2402.03570*, 2024.

Yonathan Efroni, Chi Jin, Akshay Krishnamurthy, and Sobhan Miryoosefi. Provable reinforcement learning with a short-term memory. In *International Conference on Machine Learning*, pages 5832–5850. PMLR, 2022.

Benjamin Eysenbach, Tianjun Zhang, Sergey Levine, and Russ R Salakhutdinov. Contrastive learning as goal-conditioned reinforcement learning. *Advances in Neural Information Processing Systems (NeurIPS)*, 35:35603–35620, 2022.

Norm Ferns, Prakash Panangaden, and Doina Precup. Metrics for finite markov decision processes. In *UAI*, volume 4, pages 162–169, 2004.

Chelsea Finn, Paul Christiano, Pieter Abbeel, and Sergey Levine. A connection between generative adversarial networks, inverse reinforcement learning, and energy-based models. *arXiv preprint arXiv:1611.03852*, 2016.

Scott Fujimoto, Herke Hoof, and David Meger. Addressing function approximation error in actor-critic methods. In *International Conference on Machine Learning (ICML)*, pages 1587–1596. PMLR, 2018.

Scott Fujimoto, David Meger, and Doina Precup. An equivalence between loss functions and non-uniform sampling in experience replay. *Advances in Neural Information Processing Systems (NeurIPS)*, 33:14219–14230, 2020.

Scott Fujimoto, Wei-Di Chang, Edward Smith, Shixiang Shane Gu, Doina Precup, and David Meger. For sale: State-action representation learning for deep reinforcement learning. *Advances in neural information processing systems (NeurIPS)*, 36:61573–61624, 2023.

Scott Fujimoto, Pierluca D’Oro, Amy Zhang, Yuandong Tian, and Michael Rabbat. Towards general-purpose model-free reinforcement learning, 2025. URL <https://arxiv.org/abs/2501.16142>, 2025.

Carles Gelada, Saurabh Kumar, Jacob Buckman, Ofir Nachum, and Marc G Bellemare. Deepmdp: Learning continuous latent space models for representation learning. In *International Conference on Machine Learning (ICML)*, pages 2170–2179. PMLR, 2019.

Dibya Ghosh, Chethan Anand Bhateja, and Sergey Levine. Reinforcement learning from passive data via latent intentions. In *International Conference on Machine Learning (ICML)*, pages 11321–11339. PMLR, 2023.

Jean-Bastien Grill, Florian Strub, Florent Altché, Corentin Tallec, Pierre Richemond, Elena Buchatskaya, Carl Doersch, Bernardo Avila Pires, Zhaohan Guo, Mohammad Gheshlaghi Azar, et al. Bootstrap your own latent-a new approach to self-supervised learning. *Advances in neural information processing systems*, 33:21271–21284, 2020.

Jiacheng Guo, Zihao Li, Huazheng Wang, Mengdi Wang, Zhuoran Yang, and Xuezhou Zhang. Provably efficient representation learning with tractable planning in low-rank pomdp. In *International Conference on Machine Learning (ICML)*, pages 11967–11997. PMLR, 2023.

Zhaohan Daniel Guo, Bernardo Avila Pires, Bilal Piot, Jean-Bastien Grill, Florent Altché, Rémi Munos, and Mohammad Gheshlaghi Azar. Bootstrap latent-predictive representations for multitask reinforcement learning. In *International Conference on Machine Learning (ICML)*, pages 3875–3886. PMLR, 2020.

Michael Gutmann and Aapo Hyvärinen. Noise-contrastive estimation: A new estimation principle for unnormalized statistical models. In *International Conference on Artificial Intelligence and Statistics (AISTATS)*, pages 297–304. JMLR Workshop and Conference Proceedings, 2010.

Michael U Gutmann and Aapo Hyvärinen. Noise-contrastive estimation of unnormalized statistical models, with applications to natural image statistics. *The Journal of Machine Learning Research (JMLR)*, 13(1):307–361, 2012.

David Ha and Jürgen Schmidhuber. Recurrent world models facilitate policy evolution. *Advances in Neural Information Processing Systems (NeurIPS)*, 31, 2018.

Tuomas Haarnoja, Aurick Zhou, Pieter Abbeel, and Sergey Levine. Soft actor-critic: Off-policy maximum entropy deep reinforcement learning with a stochastic actor. In *International Conference on Machine Learning (ICML)*, pages 1861–1870. Pmlr, 2018.

Danijar Hafner, Timothy Lillicrap, Jimmy Ba, and Mohammad Norouzi. Dream to control: Learning behaviors by latent imagination. *arXiv preprint arXiv:1912.01603*, 2019a.

Danijar Hafner, Timothy Lillicrap, Ian Fischer, Ruben Villegas, David Ha, Honglak Lee, and James Davidson. Learning latent dynamics for planning from pixels. In *International Conference on Machine Learning (ICML)*, pages 2555–2565. PMLR, 2019b.

Danijar Hafner, Timothy Lillicrap, Mohammad Norouzi, and Jimmy Ba. Mastering atari with discrete world models. *arXiv preprint arXiv:2010.02193*, 2020.

Danijar Hafner, Jurgis Pasukonis, Jimmy Ba, and Timothy Lillicrap. Mastering diverse domains through world models, 2024. <https://arxiv.org/abs/2301.04104>, 2023.

Nicklas Hansen, Xiaolong Wang, and Hao Su. Temporal difference learning for model predictive control. *arXiv preprint arXiv:2203.04955*, 2022.

Nicklas Hansen, Hao Su, and Xiaolong Wang. Td-mpc2: Scalable, robust world models for continuous control. *arXiv preprint arXiv:2310.16828*, 2023.

Jeff Z HaoChen, Colin Wei, Adrien Gaidon, and Tengyu Ma. Provable guarantees for self-supervised deep learning with spectral contrastive loss. arxiv e-prints, art. *arXiv preprint arXiv:2106.04156*, 2021.

Nicolas Heess, Gregory Wayne, David Silver, Timothy Lillicrap, Tom Erez, and Yuval Tassa. Learning continuous control policies by stochastic value gradients. *Advances in Neural Information Processing Systems (NeurIPS)*, 28, 2015.

Irina Higgins, Loic Matthey, Arka Pal, Christopher Burgess, Xavier Glorot, Matthew Botvinick, Shakir Mohamed, and Alexander Lerchner. beta-vae: Learning basic visual concepts with a constrained variational framework. In *International Conference on Learning Representations (ICLR)*, 2017.

Jonathan Ho, Ajay Jain, and Pieter Abbeel. Denoising diffusion probabilistic models. *Advances in Neural Information Processing Systems (NeurIPS)*, 33:6840–6851, 2020.

Yang Hu, Tianyi Chen, Na Li, Kai Wang, and Bo Dai. Primal-dual spectral representation for off-policy evaluation. *arXiv preprint arXiv:2410.17538*, 2024.

Michael Janner, Justin Fu, Marvin Zhang, and Sergey Levine. When to trust your model: Model-based policy optimization. *Advances in Neural Information Processing Systems (NeurIPS)*, 32, 2019.

Chi Jin, Zeyuan Allen-Zhu, Sébastien Bubeck, and Michael I Jordan. Is q-learning provably efficient? *Advances in Neural Information Processing Systems (NeurIPS)*, 31, 2018.

Chi Jin, Zhuoran Yang, Zhaoran Wang, and Michael I Jordan. Provably efficient reinforcement learning with linear function approximation. In *Conference on Learning Theory (CoLT)*, pages 2137–2143. PMLR, 2020.

Sanket Kamthe and Marc Deisenroth. Data-efficient reinforcement learning with probabilistic model predictive control. In *International Conference on Artificial Intelligence and Statistics*, pages 1701–1710. PMLR, 2018.

Hassan K. Khalil and Mark Minor. *Nonlinear Control*. Pearson, 2015.

Rahul Kidambi, Aravind Rajeswaran, Praneeth Netrapalli, and Thorsten Joachims. Morel: Model-based offline reinforcement learning. *Advances in Neural Information Processing Systems (NeurIPS)*, 33:21810–21823, 2020.

Kyungsoo Kim, Jeongsoo Ha, and Yusung Kim. Self-predictive dynamics for generalization of vision-based reinforcement learning. *arXiv preprint arXiv:2506.05418*, 2025.

Diederik P Kingma and Max Welling. Auto-encoding variational bayes. *arXiv preprint arXiv:1312.6114*, 2013.

Tejas D Kulkarni, Ardavan Saeedi, Simanta Gautam, and Samuel J Gershman. Deep successor reinforcement learning. *arXiv preprint arXiv:1606.02396*, 2016.

Thanard Kurutach, Ignasi Clavera, Yan Duan, Aviv Tamar, and Pieter Abbeel. Model-ensemble trust-region policy optimization. *arXiv preprint arXiv:1802.10592*, 2018.

Michael Laskin, Aravind Srinivas, and Pieter Abbeel. Curl: Contrastive unsupervised representations for reinforcement learning. In *International conference on machine learning*, pages 5639–5650. PMLR, 2020.

Yann LeCun, Sumit Chopra, Raia Hadsell, M Ranzato, Fujie Huang, et al. A tutorial on energy-based learning. *Predicting structured data*, 1(0), 2006.

Alex X Lee, Anusha Nagabandi, Pieter Abbeel, and Sergey Levine. Stochastic latent actor-critic: Deep reinforcement learning with a latent variable model. *Advances in Neural Information Processing Systems (NeurIPS)*, 33:741–752, 2020.

Hojoon Lee, Dongyoon Hwang, Donghu Kim, Hyunseung Kim, Jun Jet Tai, Kaushik Subramanian, Peter R Wurman, Jaegul Choo, Peter Stone, and Takuma Seno. Simba: Simplicity bias for scaling up parameters in deep reinforcement learning. *arXiv preprint arXiv:2410.09754*, 2024.

Sergey Levine, Aviral Kumar, George Tucker, and Justin Fu. Offline reinforcement learning: Tutorial, review, and perspectives on open problems. *arXiv preprint arXiv:2005.01643*, 2020.

Weijian Liao, Zongzhang Zhang, and Yang Yu. Policy-independent behavioral metric-based representation for deep reinforcement learning. In *Proceedings of the AAAI Conference on Artificial Intelligence (AAAI)*, volume 37, pages 8746–8754, 2023.

Jihao Long and Jiequn Han. Perturbational complexity by distribution mismatch: A systematic analysis of reinforcement learning in reproducing kernel hilbert space. *arXiv preprint arXiv:2111.03469*, 2021.

Fan-Ming Luo, Tian Xu, Hang Lai, Xiong-Hui Chen, Weinan Zhang, and Yang Yu. A survey on model-based reinforcement learning. *Science China Information Sciences*, 67(2):121101, 2024.

Yuping Luo, Huazhe Xu, Yuanzhi Li, Yuandong Tian, Trevor Darrell, and Tengyu Ma. Algorithmic framework for model-based deep reinforcement learning with theoretical guarantees. *arXiv preprint arXiv:1807.03858*, 2018.

Haitong Ma, Bo Dai, Zhaolin Ren, Yebin Wang, and Na Li. Offline imitation learning upon arbitrary demonstrations by pre-training dynamics representations. *arXiv preprint arXiv:2508.14383*, 2025.

Zhuang Ma and Michael Collins. Noise contrastive estimation and negative sampling for conditional models: Consistency and statistical efficiency. *arXiv preprint arXiv:1809.01812*, 2018.

Trevor McInroe, Lukas Schäfer, and Stefano V Albrecht. Learning temporally-consistent representations for data-efficient reinforcement learning. *arxiv preprint. arXiv preprint arXiv:2110.04935*, 2021.

Vincent Micheli, Eloi Alonso, and François Fleuret. Transformers are sample-efficient world models. *arXiv preprint arXiv:2209.00588*, 2022.

Volodymyr Mnih, Koray Kavukcuoglu, David Silver, Alex Graves, Ioannis Antonoglou, Daan Wierstra, and Martin Riedmiller. Playing atari with deep reinforcement learning. *arXiv preprint arXiv:1312.5602*, 2013.

Mattes Mollenhauer, Ingmar Schuster, Stefan Klus, and Christof Schütte. Singular value decomposition of operators on reproducing kernel hilbert spaces. In *Advances in Dynamics, Optimization and Computation: A volume dedicated to Michael Dellnitz on the occasion of his 60th birthday*, pages 109–131. Springer, 2020.

Jelle Munk, Jens Kober, and Robert Babuška. Learning state representation for deep actor-critic control. In *2016 IEEE 55th conference on decision and control (CDC)*, pages 4667–4673. IEEE, 2016.

Michał Nauman, Mateusz Ostaszewski, Krzysztof Jankowski, Piotr Miłoś, and Marek Cygan. Bigger, regularized, optimistic: scaling for compute and sample efficient continuous control. *Advances in Neural Information Processing Systems (NeurIPS)*, 37:113038–113071, 2024.

Aaron van den Oord, Yazhe Li, and Oriol Vinyals. Representation learning with contrastive predictive coding. *arXiv preprint arXiv:1807.03748*, 2018.

Long Ouyang, Jeffrey Wu, Xu Jiang, Diogo Almeida, Carroll Wainwright, Pamela Mishkin, Chong Zhang, Sandhini Agarwal, Katarina Slama, Alex Ray, et al. Training language models to follow instructions with human feedback. *Advances in neural information processing systems*, 35:27730–27744, 2022.

Marek Petrik. An analysis of laplacian methods for value function approximation in mdps. In *IJCAI*, pages 2574–2579, 2007.

Alec Radford, Jong Wook Kim, Chris Hallacy, Aditya Ramesh, Gabriel Goh, Sandhini Agarwal, Girish Sastry, Amanda Askell, Pamela Mishkin, Jack Clark, et al. Learning transferable visual models from natural language supervision. In *International Conference on Machine Learning*, pages 8748–8763. PMLR, 2021.

Ali Rahimi and Benjamin Recht. Random features for large-scale kernel machines. *Advances in Neural Information Processing Systems (NeurIPS)*, 20, 2007.

Tongzheng Ren, Tianjun Zhang, Csaba Szepesvári, and Bo Dai. A free lunch from the noise: Provably and practical exploration for representation learning. In *Uncertainty in Artificial Intelligence (UAI)*, pages 1686–1696. PMLR, 2022.

Tongzheng Ren, Chenjun Xiao, Tianjun Zhang, Na Li, Zhaoran Wang, Sujay Sanghavi, Dale Schuurmans, and Bo Dai. Latent variable representation for reinforcement learning. In *The Eleventh International Conference on Learning Representations (ICLR)*. OpenReview.net, 2023a.

Tongzheng Ren, Tianjun Zhang, Lisa Lee, Joseph E. Gonzalez, Dale Schuurmans, and Bo Dai. Spectral decomposition representation for reinforcement learning. In *The Eleventh International Conference on Learning Representations (ICLR)*. OpenReview.net, 2023b.

Zhaolin Ren, Runyu Zhang, Bo Dai, and Na Li. Scalable spectral representations for multi-agent reinforcement learning in network mdps. *arXiv preprint arXiv:2410.17221*, 2024.

Zhaolin Ren, Tongzheng Ren, Haitong Ma, Na Li, and Bo Dai. Stochastic nonlinear control via finite-dimensional spectral dynamics embedding. *IEEE Transactions on Automatic Control*, 2025.

Benjamin Rhodes, Kai Xu, and Michael U Gutmann. Telescoping density-ratio estimation. *Advances in Neural Information Processing Systems (NeurIPS)*, 33:4905–4916, 2020.

Joshua Robinson, Ching-Yao Chuang, Suvrit Sra, and Stefanie Jegelka. Contrastive learning with hard negative samples. *arXiv preprint arXiv:2010.04592*, 2020.

Max Schwarzer, Ankesh Anand, Rishab Goel, R Devon Hjelm, Aaron Courville, and Philip Bachman. Data-efficient reinforcement learning with self-predictive representations. *arXiv preprint arXiv:2007.05929*, 2020.

Dmitry Shribak, Chen-Xiao Gao, Yitong Li, Chenjun Xiao, and Bo Dai. Diffusion spectral representation for reinforcement learning. In *Advances in Neural Information Processing Systems (NeurIPS)*, 2024.

Yang Song and Diederik P Kingma. How to train your energy-based models. *arXiv preprint arXiv:2101.03288*, 2021.

Yang Song, Jascha Sohl-Dickstein, Diederik P Kingma, Abhishek Kumar, Stefano Ermon, and Ben Poole. Score-based generative modeling through stochastic differential equations. In *International Conference on Learning Representations (ICLR)*.

Adam Stooke, Kimin Lee, Pieter Abbeel, and Michael Laskin. Decoupling representation learning from reinforcement learning. In *International conference on machine learning*, pages 9870–9879. PMLR, 2021.

Yihao Sun, Jiaji Zhang, Chengxing Jia, Haoxin Lin, Junyin Ye, and Yang Yu. Model-bellman inconsistency for model-based offline reinforcement learning. In *International Conference on Machine Learning (ICML)*, pages 33177–33194. PMLR, 2023.

Richard S Sutton, Andrew G Barto, et al. *Reinforcement learning: An introduction*, volume 1. MIT press Cambridge, 1998.

Chen Tang, Ben Abbatematteo, Jiaheng Hu, Rohan Chandra, Roberto Martín-Martín, and Peter Stone. Deep reinforcement learning for robotics: A survey of real-world successes. In *Proceedings of the AAAI Conference on Artificial Intelligence*, volume 39, pages 28694–28698, 2025.

Yunhao Tang, Zhaohan Daniel Guo, Pierre Harvey Richemond, Bernardo Avila Pires, Yash Chandak, Rémi Munos, Mark Rowland, Mohammad Gheshlaghi Azar, Charline Le Lan, Clare Lyle, et al. Understanding self-predictive learning for reinforcement learning. In *International Conference on Machine Learning (ICML)*, pages 33632–33656. PMLR, 2023.

Yuval Tassa, Yotam Doron, Alistair Muldal, Tom Erez, Yazhe Li, Diego de Las Casas, David Budden, Abbas Abdolmaleki, Josh Merel, Andrew Lefrancq, et al. Deepmind control suite. *arXiv preprint arXiv:1801.00690*, 2018.

Ahmed Touati and Yann Ollivier. Learning one representation to optimize all rewards. *Advances in Neural Information Processing Systems (NeurIPS)*, 34:13–23, 2021.

Masatoshi Uehara, Xuezhou Zhang, and Wen Sun. Representation learning for online and offline rl in low-rank mdps. *arXiv preprint arXiv:2110.04652*, 2021.

Jiyi Wang, Jingyang Ke, Bo Dai, and Anqi Wu. Learning task-agnostic skill bases to uncover motor primitives in animal behaviors. *arXiv preprint arXiv:2506.15190*, 2025.

Tingwu Wang, Xuchan Bao, Ignasi Clavera, Jerrick Hoang, Yeming Wen, Eric Langlois, Shunshi Zhang, Guodong Zhang, Pieter Abbeel, and Jimmy Ba. Benchmarking model-based reinforcement learning. *arXiv preprint arXiv:1907.02057*, 2019.

Yifan Wu, George Tucker, and Ofir Nachum. The laplacian in rl: Learning representations with efficient approximations. *arXiv preprint arXiv:1810.04586*, 2018.

Jiannan Xiang, Yi Gu, Zihan Liu, Zeyu Feng, Qiyue Gao, Yiyan Hu, Benhao Huang, Guangyi Liu, Yichi Yang, Kun Zhou, et al. Pan: A world model for general, interactable, and long-horizon world simulation. *arXiv preprint arXiv:2511.09057*, 2025.

Kai Yang, Jian Tao, Jiafei Lyu, Chunjiang Ge, Jiaxin Chen, Weihan Shen, Xiaolong Zhu, and Xiu Li. Using human feedback to fine-tune diffusion models without any reward model. In *Proceedings of the IEEE/CVF Conference on Computer Vision and Pattern Recognition (CVPR)*, pages 8941–8951, 2024.

Lin Yang and Mengdi Wang. Reinforcement learning in feature space: Matrix bandit, kernels, and regret bound. In *International Conference on Machine Learning (ICML)*, pages 10746–10756. PMLR, 2020.

Zhuoran Yang, Chi Jin, Zhaoran Wang, Mengdi Wang, and Michael I Jordan. On function approximation in reinforcement learning: Optimism in the face of large state spaces. *Advances in Neural Information Processing Systems (NeurIPS)*, 2020, 2020.

Hengshuai Yao, Csaba Szepesvári, Bernardo Avila Pires, and Xinhua Zhang. Pseudo-mdps and factored linear action models. In *2014 IEEE Symposium on Adaptive Dynamic Programming and Reinforcement Learning (ADPRL)*, pages 1–9. IEEE, 2014.

Denis Yarats, Rob Fergus, Alessandro Lazaric, and Lerrel Pinto. Mastering visual continuous control: Improved data-augmented reinforcement learning. *arXiv preprint arXiv:2107.09645*, 2021a.

Denis Yarats, Ilya Kostrikov, and Rob Fergus. Image augmentation is all you need: Regularizing deep reinforcement learning from pixels. In *International Conference on Learning Representations (ICLR)*, 2021b.

Denis Yarats, Amy Zhang, Ilya Kostrikov, Brandon Amos, Joelle Pineau, and Rob Fergus. Improving sample efficiency in model-free reinforcement learning from images. In *Proceedings of the AAAI Conference on artificial intelligence (AAAI)*, volume 35, pages 10674–10681, 2021c.

Tao Yu, Zhizheng Zhang, Cuiling Lan, Yan Lu, and Zhibo Chen. Mask-based latent reconstruction for reinforcement learning. *Advances in Neural Information Processing Systems (NeurIPS)*, 35: 25117–25131, 2022.

Tianhe Yu, Garrett Thomas, Lantao Yu, Stefano Ermon, James Y Zou, Sergey Levine, Chelsea Finn, and Tengyu Ma. Mopo: Model-based offline policy optimization. *Advances in Neural Information Processing Systems (NeurIPS)*, 33:14129–14142, 2020.

Hongming Zhang, Tongzheng Ren, Chenjun Xiao, Dale Schuurmans, and Bo Dai. Provable representation with efficient planning for partially observable reinforcement learning. In *International Conference on Machine Learning (ICML)*.

Tianjun Zhang, Tongzheng Ren, Mengjiao Yang, Joseph Gonzalez, Dale Schuurmans, and Bo Dai. Making linear mdps practical via contrastive representation learning. In *International Conference on Machine Learning (ICML)*, volume 162 of *Proceedings of Machine Learning Research*, pages 26447–26466. PMLR, 2022.

Ruijie Zheng, Xiayao Wang, Yanchao Sun, Shuang Ma, Jieyu Zhao, Huazhe Xu, Hal Daumé III, and Furong Huang. TACO: Temporal latent action-driven contrastive loss for visual reinforcement learning. *Advances in Neural Information Processing Systems (NeurIPS)*, 36:48203–48225, 2023.

Sirui Zheng, Lingxiao Wang, Shuang Qiu, Zuyue Fu, Zhuoran Yang, Csaba Szepesvari, and Zhaoran Wang. Optimistic exploration with learned features provably solves markov decision processes with neural dynamics. In *International Conference on Learning Representations (ICLR)*, 2022.

Gaoyue Zhou, Hengkai Pan, Yann LeCun, and Lerrel Pinto. Dino-wm: World models on pre-trained visual features enable zero-shot planning 2024. *URL <https://arxiv.org/abs/2411.4983>*.

A Online Exploration with Spectral Representations

Following [Guo et al. \[2023\]](#), with the estimation of $\hat{\phi}_n$ at the n -th episode, we introduce the bonus term $\hat{b}_n(s, a)$ to implement the principle of optimism in the face of uncertainty. However, since our representation lies in the kernel space \mathcal{H}_k , we follow [Yang et al. \[2020\]](#) and define the bonus function in terms of the kernel:

$$\hat{b}_n(s, a) = \alpha_n \lambda^{-1/2} \cdot \left(\hat{K}_{(s,a),(s,a)}^{(n)} - \hat{K}_{(s,a)}^{(n)\top} \left(\hat{K}^{(n)} + \lambda I \right) \hat{K}_{(s,a)}^{(n)} \right)^{1/2}, \quad (54)$$

where

$$\begin{aligned} \hat{K}_{(s,a),(s,a)}^{(n)} &= \langle \hat{\phi}_n(s, a), \hat{\phi}_n(s_i, a_i) \rangle_{\mathcal{H}_k} \in \mathbb{R}, \\ \hat{K}_{(s,a)}^{(n)} &= [\langle \hat{\phi}_n(s, a), \hat{\phi}_n(s_i, a_i) \rangle_{\mathcal{H}_k}]_{i \in [\mathcal{D}_n]} \in \mathbb{R}^{|\mathcal{D}_n|}, \\ \hat{K}^{(n)} &= [\langle \hat{\phi}_n(s_i, a_i), \hat{\phi}_n(s_j, a_j) \rangle_{\mathcal{H}_k}]_{i,j \in [\mathcal{D}_n]} \in \mathbb{R}^{|\mathcal{D}_n| \times |\mathcal{D}_n|}. \end{aligned} \quad (55)$$

The bonus function is added to the extrinsic reward and used for planning in the approximated dynamics to learn optimistic Q -values that upper-bound the true Q -values. The optimistic version of our algorithm, which incorporate such bonus functions, is defined in [Algorithm 2](#). Note that this algorithm is only leveraged for theoretical analysis, but not for actual implementations.

Algorithm 2 Optimistic Online Reinforcement Learning with Spectral Representations

Initialize: replay buffer $\mathcal{D}_0 = \emptyset$, $\pi_0 = \mathcal{U}(\mathcal{A})$

- 1: **for** episode $n = 1, 2, \dots, N$ **do**
- 2: Collect the transitions (s_h, a_h, s_{h+1}, r_h) following $a_h \in \mathcal{U}(\mathcal{A})$, $s_{h+1} \sim \mathbb{P}(\cdot | s_h, a_h)$, $r_h = r(s_h, a_h)$
- 3: $\mathcal{D}_n \leftarrow \mathcal{D}_{n-1} \cup \{(s_h, a_h, s_{h+1}, r_h)\}_{h=1}^H$
- 4: Learn the spectral representations $\hat{\phi}_n$ and $\hat{\mu}_n$ using \mathcal{D}_n
- 5: Specify the exploration bonus function $\hat{b}(s, a)$ as [\(54\)](#)
- 6: Update $\pi_n = \text{argmax}_{\pi} V_{\hat{\mathbb{P}}, r + \hat{b}_n}^{\pi}$, where $V_{\hat{\mathbb{P}}, r + \hat{b}_n}^{\pi}$ is the value function of π with approximated dynamics $\hat{\mathbb{P}}_n = \langle \hat{\phi}_n, \hat{\mu}_n \rangle_{\mathcal{H}_k}$ and augmented reward function $r + \hat{b}_n$
- 7: **end for**
- Return** $\pi_1, \pi_2, \dots, \pi_N$

B Implementation Details

In this section, we introduce the implementation details of each algorithm in our empirical evaluation section. In [Table 2](#), we list the common hyperparameters that are shared across most of the algorithms in this paper. For details about each specific algorithm, we will detail below.

B.1 Implementation Details of Baseline Algorithms

Configurations of TD3 [\[Fujimoto et al., 2018\]](#). Due to its simplicity and strong empirical performance, we re-implemented TD3 in our code repository and built all spectral representation-based algorithms on TD3. The hyperparameters that we used to obtain the results are listed in [Table 3](#).

Table 2: Hyperparameters shared across different algorithms.

Parameter	Proprioceptive	Visual
frame skip	2	2
frame stack	1	3
buffer size	1,000,000	1,000,000
batch size	512	256
train frames	1,000,000	1,000,000
warmup frames	10,000	4000
discounting factor γ	0.99	0.99
n -step TD	1	3

Note that we tuned certain design choices (such as target network update strategy) and hyperparameters based on our observation on the DMControl suite, and therefore, the final choice may slightly differ from the original implementation.

Table 3: Hyperparameters specific for TD3.

Parameter	Value
actor network	MLP(dim(S), 512, 512, 512, dim(A))
critic network	MLP(dim(S)+dim(A), 512, 512, 512, 1)
learning rate	0.0003
soft update	True
soft update rate τ	0.005
target update interval	1
actor update interval	1
policy noise	0.2
noise clip	0.3
exploration noise	0.2

Configurations of SAC [Haarnoja et al., 2018]. Compared to TD3, SAC introduces the principle of maximum entropy into reinforcement learning and regularizes the traditional RL objective with entropy. Empirically, entropy regularization encourages the policy to explore the environment, thus potentially leading to improved performance. The hyperparameters of SAC are listed in Table 4. We enable the automatic tuning of the coefficient of the entropy term and set the target entropy to $-\dim(\mathcal{A})$ by default.

Configurations of TD7 [Fujimoto et al., 2023]. TD7 incorporates several improvements over TD3, including representation learning by embedding prediction, 2) policy checkpointing, behavior cloning regularization for offline scenarios, and LAP replay buffer [Fujimoto et al., 2020]. Different from how we leverage spectral representations, TD7 feeds the representations alongside with the raw observations and actions into the value networks. We re-implemented the TD7 algorithm for

Table 4: Hyperparameters specific for SAC.

Parameter	Value
actor network	$\text{MLP}(\text{dim}(\mathbf{S}), 512, 512, 512, 2\text{dim}(\mathbf{A}))$
critic network	$\text{MLP}(\text{dim}(\mathbf{S}) + \text{dim}(\mathbf{A}), 512, 512, 512, 1)$
learning rate	0.0003
soft update	True
soft update rate τ	0.005
target update interval	1
auto entropy	True, with target as $-\text{dim}(\mathbf{A})$

DMControl tasks and used the recommended hyperparameters in the author-provided implementation, which are listed in Table 5.

Table 5: Hyperparameters specific for TD7.

Parameter	Value
embedding dimension	256
hidden dimension	256
learning rate	0.0003
target update interval	250
actor update interval	1
policy noise	0.2
noise clip	0.5
exploration noise	0.1
LAP α	0.4
LAP max priority reset interval	250

Configurations of DrQ-V2 [Yarats et al., 2021a]. DrQ-V2 is a model-free reinforcement learning algorithm designed to efficiently solve complex control tasks by directly learning from raw pixel data. The core innovation of DrQ-V2 is to apply image augmentation to the raw observations of the agents to regularize the visual encoders, therefore preventing divergent optimization due the challenge of learning from pixels. Although the official implementation of DrQ-V2 uses different sets of hyperparameters for varying task difficulties, we used identical hyperparameters for all tasks in our experiments. The hyperparameters are listed in Table 6.

Configurations of Dreamer-V3 [Hafner et al., 2023]. Dreamer-V3 is a general and highly performant model-based reinforcement learning algorithm. Its core concept is to first learn an RSSM that predicts the future latent states based on past observations and actions, thus enabling efficient simulation within the latent space. The agent then learns optimal behaviors through imaginary interaction with this learned simulation, rather than through slow and costly real-world interaction. Such a model-based approach makes it incredibly data-efficient compared to model-free

Table 6: Hyperparameters specific for **DrQ-V2**.

Parameter	Value
actor hidden dimension	1024
critic hidden dimension	1024
embedding dimension	50
actor std schedule	<code>linear(1.0, 0.1, 500000)</code>
actor std clip	0.3
critic loss	Mean Squared Error (MSE)
learning rate	0.0001
network update interval	2
network soft update rate	0.01

methods. For our experiments, we used existing PyTorch implementation of **Dreamer-V3** provided in <https://github.com/NM512/dreamerv3-torch> and adapted it for our evaluation protocol.

Configurations of TDMPC2 [Hansen et al., 2023]. TDMPC2 is another representative model-based reinforcement learning algorithm. Compared to Dreamer-V3, TDMPC2 learns a light-weight latent space dynamics model by predicting the representations of the next observations using the representation of current observations and actions. Another innovation of TDMPC2 is that, it incorporates model predictive control during sampling to actively explore the environments based on the current estimation of the model. This design significantly improves the undirectional exploration strategy used in common RL algorithms, and boosts sample efficiency. Similarly, we re-used the author provided PyTorch implementation and configurations in <https://github.com/nicklashansen/tdmpc2>, and only made modifications to adapt it for our evaluation protocol.

B.2 Implementation Details of Spectral Representation-Based Algorithms

In this section we disclose the details about the spectral representation-based algorithms. We build all these algorithms upon TD3, with the only difference being that the critic networks take the spectral representations as input. Therefore, we will primarily focus on the representation learning part. Besides, since many of our algorithms involve perturbations, we normalize the observation by its mean and standard deviation to keep it on a similar scale of the Gaussian noise.

In our implementation, we extensively use **ResidualMLP**, a variant of **MLP** layers with residual connections, since we find it consistently demonstrates better plasticity and expressiveness, echoing the recent findings by Nauman et al. [2024] and Lee et al. [2024]. A diagram of this architecture is provided in Figure 10.

Configurations of Speder . **Speder** employs a linear spectral formulation and uses the spectral contrastive learning to optimize the representations. Since in essence it is still performing contrastive learning, we also employ the noise perturbation technique for **Speder** to regularize the contrastive learning from degeneration. We also use a target network for the representation networks, whose update rate is 0.01. The configurations of **Speder** are listed in Table 7.

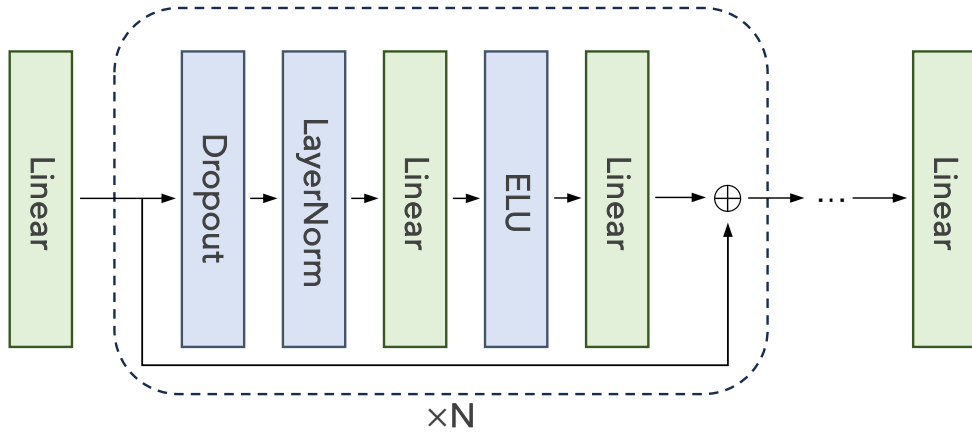


Figure 10: Illustration of the residual MLP network.

Table 7: Hyperparameters specific for Speder.

Parameter	Value
representation dimension d_r	512
representation learning rate	0.000005
representation target update rate	0.01
noise embedding dimension d_n	128
architecture of φ	<code>ResidualMLP(dim(S)+dim(A), 512, 512, d_r)</code>
architecture of ν	<code>ResidualMLP(dim(S)+d_n, 512, 512, d_r)</code>
number of noise levels	25
reward prediction loss weight	0.1

Configurations of LV-Rep . LV-Rep uses a standard VAE architecture but with a learnable prior distribution. To prevent regularizing the posterior distribution with a bad prior in the initial stage of training, Hafner et al. [2020] applies decoupled and asymmetric KL regularization for the posterior and prior. However, in our experiments, we found this provides marginal benefits to the performance, and therefore we use a balanced regularization by default. The configurations of LV-Rep are listed in Table 8.

Table 8: Hyperparameters specific for LV-Rep.

Parameter	Value
representation dimension d_r	512
representation learning rate	0.0001
representation target update rate	0.005
distribution of the latent	diagonal Gaussian
architecture of decoder	$\text{MLP}(2 * \text{dim}(\mathcal{S}) + \text{dim}(\mathcal{A}), 512, 512, 512, 2 * d_r)$
architecture of decoder	$\text{MLP}(d_r, 512, 512, 512, \text{dim}(\mathcal{S}))$
architecture of the prior	$\text{MLP}(\text{dim}(\mathcal{S}) + \text{dim}(\mathcal{A}), 512, 512, d_r)$
minimum log std	-20
maximum log std	2.0
coefficient for KL β	0.1
reward prediction loss weight	0.05

Configurations of Diff-SR (with proprioceptive observation) . In Diff-SR, we are learning a series of score functions of noise-perturbed distributions and extracting the spectral representations from $\nabla_{\tilde{s}'} \log \mathbb{P}(\tilde{s}'|s, a; \beta) = \varphi_\theta(s, a)^\top \nabla_{\tilde{s}'} \nu_\theta(\tilde{s}'; \beta)$. Instead of parameterizing $\nu_\theta(\tilde{s}'; \beta)$ and taking the second order for optimization, we directly parameterize $\nabla_{\tilde{s}'} \nu_\theta(\tilde{s}'; \beta)$ as a neural network with output dimension $d_r \times \text{dim}(\mathcal{S})$, thus its inner product with $\varphi(s, a)$ gives the score estimation. Finally, the configurations of Diff-SR are provided in Table 9.

Table 9: Hyperparameters specific for Diff-SR.

Parameter	Value
representation dimension d_r	512
representation learning rate	0.0001
representation target update rate	0.005
noise embedding dimension d_n	128
random Fourier feature N	512
architecture of φ	$\text{ResidualMLP}(\text{dim}(\mathcal{S}) + \text{dim}(\mathcal{A}), 512, 512, 512, d_r)$
architecture of $\nabla \nu$	$\text{ResidualMLP}(\text{dim}(\mathcal{S}) + d_n, 512, 512, 512, d_r \times \text{dim}(\mathcal{S}))$
number of noise levels	50
reward prediction loss weight	0.1

Configurations of CTRL-SR (with proprioceptive observation) . Similar to Diff-SR, we conduct noise contrastive learning across different levels of noise perturbations. The configurations of CTRL-SR are listed in Table 10.

Table 10: Hyperparameters specific for CTRL-SR.

Parameter	Value
representation dimension d_r	512
representation learning rate	0.0001
representation target update rate	0.005
noise embedding dimension d_n	128
random Fourier feature N	512
architecture of φ	ResidualMLP(dim(S)+dim(A), 512, 512, d_r)
architecture of $\nabla \nu$	ResidualMLP(dim(S)+ d_n , 512, 512, d_r)
number of noise levels	25
reward prediction loss weight	0.1

Adaptation of CTRL-SR and Diff-SR for visual observations. To address the challenge posed by the high dimensionality of visual observations, we employ a hierarchical strategy for both CTRL-SR and Diff-SR. Instead of performing contrastive learning or score matching directly in the raw pixel space, we first use a lightweight image encoder E_θ to project the images into compact latent embeddings, which are then used for representation learning. Due to frame stacking, the final embedding used for representation learning is a concatenation of the latent embeddings of each individual frame. For CTRL-SR, this approach works effectively. However, for Diff-SR, it may converge to a trivial constant embedding for all possible (s, a) and s' . To prevent such representation collapse, we introduce an additional reconstruction and variance-preserving objective for Diff-SR:

$$\begin{aligned} \ell_{\text{recon}}(\theta) &= \mathbb{E}_{o \sim \mathcal{D}} [\|D_\theta(E_\theta(o)) - o\|^2], \\ \ell_{\text{vp}}(\theta) &= \mathbb{E}_{\{o_i\}_{i=1}^B \sim \mathcal{D}} \left[\frac{1}{d} \sum_{j=1}^d \max(0, 1 - \text{std}(\{E_\theta(o_i)_j\}_{i=1}^B)) \right], \end{aligned} \quad (56)$$

where d_r is the representation dimension, E_θ and D_θ are the image encoder and decoder, respectively. Furthermore, we incorporate image augmentations following DrQ-V2, which helps the visual encoder develop richer and more robust representations. Specifically, for CTRL-SR, we apply image augmentations to both the observation and next observation during contrastive learning, while for Diff-SR, augmentations are applied when training the encoder by feeding augmented images and reconstructing the corresponding clean images. Additional configuration details are provided in Table 11 and Table 12.

Table 11: Hyperparameters for CTRL-SR with visual observations.

Parameter	Value
actor hidden dimension	1024
critic hidden dimension	1024
actor learning rate	0.0003
critic learning rate	0.0003
number of noise levels	50
representation dimension d_r	512
representation learning rate	0.0001
representation target update rate	0.0005
encoder dimension d_e	512
noise embedding dimension d_n	128
random Fourier feature N	512
architecture of φ	ResidualMLP($d_e + \text{dim}(A)$, 512, 512, d_r)
architecture of ν	ResidualMLP($d_e + d_n$, 512, 512, d_r)
reward prediction loss weight	0.1
weight decay	0.0001

Table 12: Hyperparameters for Diff-SR with visual observations.

Parameter	Value
actor hidden dimension	1024
critic hidden dimension	1024
actor learning rate	0.0003
critic learning rate	0.0003
number of noise levels	50
representation dimension d_r	512
representation learning rate	0.0001
representation target update rate	0.01
encoder dimension d_e	256
noise embedding dimension d_n	128
random Fourier feature N	512
architecture of φ	ResidualMLP($d_e + \text{dim}(A)$, 1024x4, d_r)
architecture of ν	ResidualMLP($d_e + d_n$, 1024x4, d_r)
reward prediction loss weight	10.0
weight decay	0.0001
ℓ_{recon} loss weight	1.0
ℓ_{vp} loss weight	0.1